nature communications

Article

https://doi.org/10.1038/s41467-025-58075-z

Wearable flexible ultrasound microneedle patch for cancer immunotherapy

Received: 21 August 2024

Accepted: 5 March 2025

Published online: 18 March 2025

Check for updates

Haoyue Xue[1,7], Jing Jin[2,7], Xing Huang[1], Zhi Tan[1], Yushun Zeng[3], Gengxi Lu[3], Xin Hu[2], Keliang Chen[2], Yonglin Su[4], Xiaolin Hu[5], Xingchen Peng[2] ✉, Laiming Jiang[1] ✉ & Jiagang Wu[1,6] ✉

Clinical approaches for cancer therapy face several interrelated challenges involving inefficient drug delivery, potential adverse side effects, and inconvenience. Here, we present an integrated wearable flexible ultrasound microneedle patch (wf-UMP) that serves as a portable platform for convenient, efficient, and minimally invasive cancer therapy. The wf-UMP adopts an all-in-one bioelectronic concept, which integrates a stretchable lead-free ultrasound transducer array for acoustic emission, a bioadhesive hydrogel elastomer for robust adhesion and acoustic coupling, and a dissolvable microneedle patch loaded with biocompatible piezoelectric nanoparticles for painless drug delivery and reactive oxygen species generation. With soft mechanical properties and enhanced electromechanical performance, wf-UMP can be robustly worn on curved and dynamic tissue surfaces for easy and effective manipulation. In preclinical studies involving mice, wf-UMP demonstrated notable anticancer effects by inducing tumor cell apoptosis, amplifying oxidative stress, and modulating immune cell proliferation. Furthermore, the synergistic immunotherapy induced by wf-UMP and Anti-PD1 further improved anticancer immunity by activating immunogenic cell death and regulating macrophages polarization, inhibiting distant tumor growth and tumor recurrence.

Cancer, or malignant tumor, remains a critical global health challenge and a leading contributor to the global disease burden, according to the World Health Organization[1]. Clinical approaches to cancer treatment primarily include surgical removal, radio/chemotherapy, targeted therapy, and immunotherapy. Despite significant advancements, cancer remains difficult to cure[1]. Nevertheless, several interrelated challenges pertaining to current clinical protocols lead to restricted use and limited therapeutic efficacy, including inconvenience, potential adverse side effects, and inefficient drug delivery[2,3]. Piezocatalytic therapy (PCT) is an emerging reactive oxygen species (ROS)-driven dynamic therapeutic strategy that relies on ultrasound (US)-activated anisotropic piezocatalysts with built-in electric fields, resulting in the generation of ROS and catalytic behavior[4]. In contrast to other dynamic therapies, PCT overcomes the penetration limits of conventional photodynamic therapy in the treatment of some deep tumors due to the deep tissue penetration nature of US. Additionally, PCT effectively generates ROS without relying on external oxygen, superior to chemodynamic therapy in hypoxic tumors[5,6]. PCT is a promising emerging technology with additional advantages that are still being researched. With the advances in nanomedicine, PCT based on piezoelectric nanoparticles (PNPs) offers potential advantages in precision over conventional radio/chemotherapy, making it a

[1]College of Materials Science and Engineering, Sichuan University, Chengdu 610064, China. [2]Department of Biotherapy, Cancer Center, West China Hospital, Sichuan University, Chengdu 610041, China. [3]Alfred E. Mann Department of Biomedical Engineering, Viterbi School of Engineering, University of Southern California, Los Angeles, CA 90089, USA. [4]Department of Rehabilitation, Cancer Center, West China Hospital, Sichuan University, Chengdu 610041, China. [5]West China School of Nursing, West China Hospital, Sichuan University, Chengdu 610041, China. [6]College of Physics, Sichuan University, Chengdu 610041, China. [7]These authors contributed equally: Haoyue Xue, Jing Jin. ✉e-mail: pxx2014@scu.edu.cn; laimingjiang@scu.edu.cn; msewujg@scu.edu.cn

https://doi.org/10.1038/s41467-025-58075-z

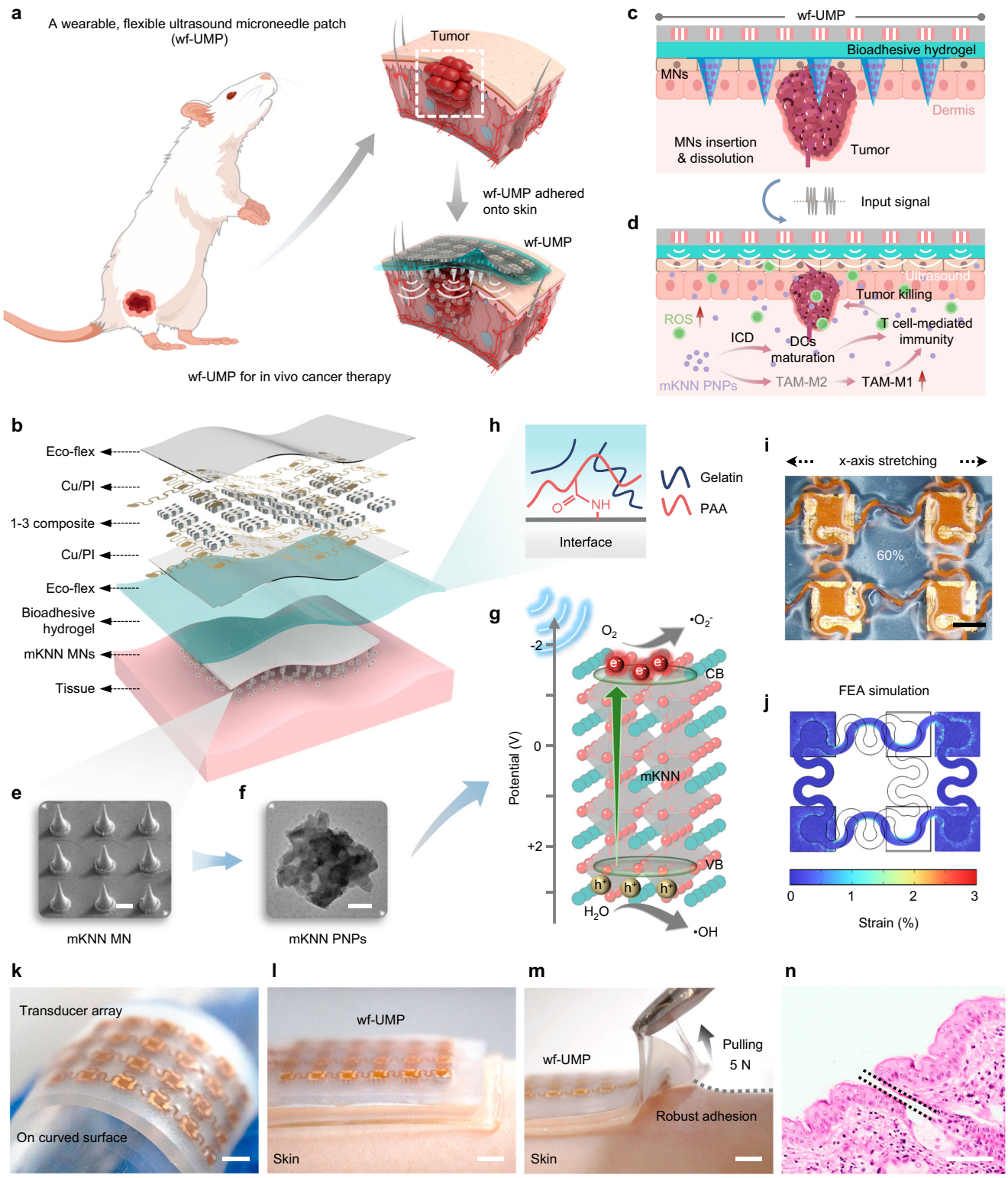

Fig. 1 | Overview of wf-UMP. a Schematic illustration of wf-UMP application for cancer therapy. Created by figdraw.com. **b** Schematic of the integrated system-level wf-UMP electronics, consisting of a flexible US transducer array for effective US emission, a bioadhesive hydrogel elastomer for robust adhesion and acoustic coupling layer, and a mKNN PNPs-loaded MN patch for drug delivery. **c**, **d** Schematic illustration of the operational procedure of wf-UMP for tumor immunotherapy. Step 1: Insertion and dissolution of MNs (**b**). Step 2: Diffusion of mKNN PNPs and ROS generation under US stimulation, along with activation of systemic immune responses (**c**). **e** SEM image of mKNN MN. Scale bar, 100 μm. **f** TEM image of mKNN PNPs. Scale bar, 50 nm. **g** Schematic illustration of the generation of ROS by mKNN PNPs under US stimulation. **h** Schematic illustration of the robust adhesion of the bioadhesive hydrogel via amide bond formation at the interface. **i**, **j** Mechanical properties of the US transducer array under tensile stress, demonstrated by experimentally stretching the transducer array (**i**) and corresponding FEA simulated strains (**j**). Scale bar, 2.5 mm. **k** Photograph of the US transducer array adhering to curved surfaces, showing its mechanical flexibility. Scale bar, 4 mm. **l** Photograph of wf-UMP adhered seamlessly on skin. Scale bar, 5 mm. **m** Photograph demonstrating the robust adhesion of wf-UMP with skin. Scale bar, 5 mm. **n** H&E staining of mouse skin after the insertion of MNs. Scale bar, 100 μm.

https://doi.org/10.1038/s41467-025-58075-z

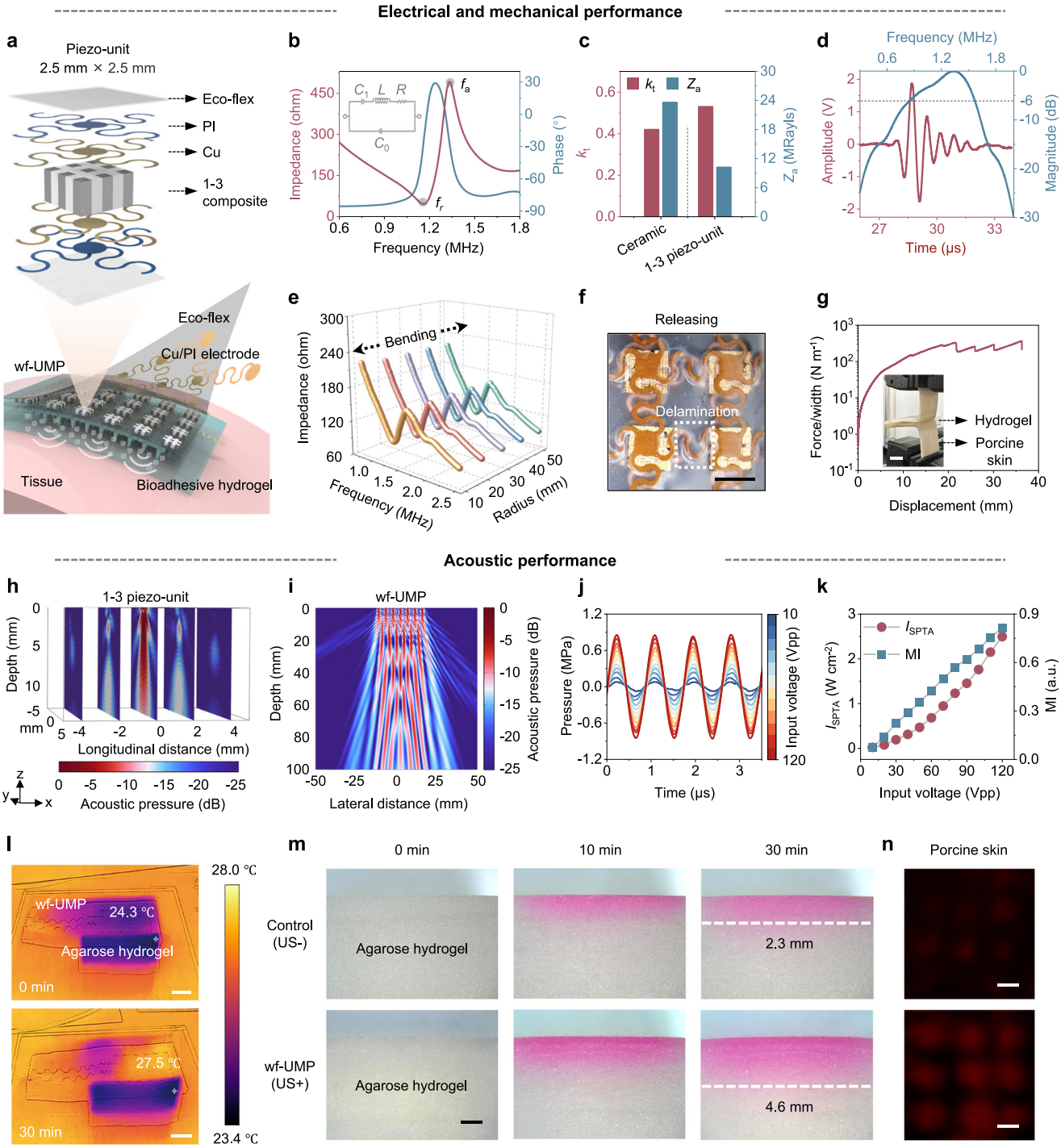

Fig. 2 | Electrical, mechanical, and acoustic performance validation of wf-UMP. **a** Schematic illustration of the active 1–3 piezo-unit in wf-UMP for US emission. **b** Impedance and phase angle spectra of 1–3 piezo-unit. The two peaks in the impedance spectrum are defined as the resonance frequency (f_r) and the anti-resonance frequency (f_a), respectively. Inset presents the equivalent RLC circuit for 1–3 piezo-unit. **c** Comparison of thickness-mode electromechanical coupling coefficient and acoustic impedance between mKNN ceramic and its 1–3 piezo-unit. **d** Pulse-echo response and frequency spectrum of the 1–3 piezo-unit. **e** Impedance spectra of wf-UMP under different bending curvatures. **f** Optical image of a 2 × 2 array released from the 80% *x*-axis tensile strain. Scale bar, 2.5 mm. **g** 180° peeling test of the bioadhesive hydrogel on porcine skin. Scale bar, 1 cm. **h** FEA simulation of the acoustic field generated by a 1–3 piezo-unit. **i** FEA simulation of the acoustic field generated by wf-UMP. **j** Acoustic pressure of wf-UMP with increasing input voltages. **k** I_{SPTA} and MI values of wf-UMP with increasing input voltages. **l** Thermal images of wf-UMP on an agarose hydrogel operated continuously for 30 min. Top, 0 min. Bottom: 30 min. Scale bars, 1 cm. **m** Comparison of drug delivery performance of wf-UMP on agarose hydrogels with/without US stimulation. Scale bars, 2 mm. **n** Confocal microscopy images of porcine skin treated with Rho B labeled wf-UMP with/without US stimulation at a depth of 328 μm. Scale bars, 250 μm.

favorable platform for cancer immunotherapy[6–8]. For therapeutic purposes, these PNPs are commonly injected into the body, but this procedure might cause discomfort, pain, and potential tissue damage. An emerging transdermal drug delivery approach, dissolvable microneedle (MN) patch, offers a minimally invasive manner to bypass the skin barrier by creating microchannels that allow loaded drugs to act locally on superficial tumors or enter the systemic circulation for further distribution. Notably, the diameter, height, and density of MNs are adjustable for painless insertion and for improved and expanded drug delivery[9,10]. However, challenges persist, including limited penetration depth, uneven drug distribution, and the difficulty in achieving adequate therapeutic doses for deeper or larger tumors. Additionally, the clinical translation of most piezocatalyst-loaded MNs is hindered by the cumulative toxicity of heavy metals and the risk of foreign body rejection.

For PCT, US, known for its high tissue penetration and biosafety, is also essential for diffusing and activating PNPs. Commonly used US transducers are rigid probes that pose challenges in effectively coupling with skin for US propagation, thus requiring the use of abundant coupling agents and needing to apply pressure to achieve effective acoustic contact on curved body parts[11,12]. Meanwhile, this procedure relies on hand-held manipulation or mechanical fixation devices (for example, straps and tapes) to hold bulky probes to the skin[13]. These hamper the ease, comfort, and continuity of the treatment. Moreover, most commercial US probes are developed using toxic lead zirconate titanate (PZT) ceramics, raising concerns about the harm to the body, especially being used as the wearable/implantable electronics[11–19]. Wearable, flexible, and lead-free US devices possess extraordinary mechanical and acoustic properties for stable and effective treatment or monitoring over time without the need of coupling agents and external fixation, especially with their biocompatibility. We hypothesize that an all-in-one wearable US-MN device incorporating flexible, lead-free US transducers and dissolvable MN patches can address the comprehensive challenges posed by current PCT. However, it remains a noteworthy challenge to realize such high-level integrated and functional wearable electronics, yet with an applicable paradigm for cancer immunotherapy.

In this work, we present a fundamental methodology for integrating wearable flexible ultrasound microneedle patches (wf-UMP) from materials engineering, device architecture and system integration (Fig. 1a), which can serve as a portable platform for cancer therapy. Distinguished from the reported studies, the wf-UMP does not rely on traditional PCT programs but adopts an US-MN all-in-one concept, which comprises three main components: (1) a stretchable conformal lead-free US transducer array for US emission, (2) a bioadhesive hydrogel elastomer containing N-hydroxysuccinimide (NHS) for robust adhesion (interfacial toughness >500 J m^{-2}) and acoustic coupling (acoustic impedance ~1.54 MRayl), and (3) a biocompatible PNPs-loaded dissolvable hyaluronic acid (HA) MN patch for minimally invasive and painless drug delivery. The wf-UMP with soft mechanical properties and enhanced electromechanical performance can be robustly worn on curved and dynamic tissue surfaces, exhibiting efficient acoustic emission, enhanced drug delivery, and improved generation of ROS. In preclinical experiments, wf-UMP demonstrated notable anticancer effects by inducing tumor cell apoptosis, amplifying oxidative stress, and modulating immune cell proliferation. RNA sequencing analysis revealed that the cytokine-cytokine receptor interaction and T cell receptor signaling pathway were upregulated with wf-UMP treatment. Moreover, the synergistic immunotherapy induced by wf-UMP and Anti-PD1 further improved anticancer immunity and effectively targeted distal cancers in dual tumor models by further activating dendritic cells (DCs) maturation through immunogenic cell death (ICD) and up-regulating macrophage M1 phenotype polarization, while augmenting antitumor immune memory to prevent tumor recurrence.

Results

Design of wf-UMP

The idea of the integrated wf-UMP for cancer therapy is illustrated in Fig. 1a, which adapts to the tumor site and enables portable treatment with minimal activity restrictions. The device orderly integrates a stretchable conformal transducer array for US emission, a bioadhesive hydrogel elastomer for robust adhesion and acoustic coupling, and a dissolving MN patch for drug delivery (Fig. 1b and Supplementary Fig. 1). Upon wf-UMP apposition, the soluble MN patch punctures the skin and dissolves, subsequently releasing loaded PNPs, which accelerates diffusion and generates ROS for tumor therapy under US stimulation, further inducing improved anticancer immunity (Fig. 1c, d).

The cone shaped MNs with a height of 600 μm, a base diameter of 250 μm, and an inter-needle spacing of 550 μm were evenly arranged in a 20 × 20 array over an area of 10 mm × 10 mm, enabling effective penetration of the skin and access to the dermis (Fig. 1e and Supplementary Figs. 2–5)[20,21]. The relatively thin backing film (~50 μm) of the MN patch ensures sufficient structural support for the MNs without exerting significant mechanical resistance during insertion (Supplementary Fig. 6). The loaded chemically modified $0.95K_{0.48}Na_{0.52}Nb_{0.97}Sb_{0.03}O_3$-$0.05Bi_{0.5}Na_{0.5}ZrO_3$-0.2% Fe_2O_3 (abbreviated as mKNN, Supplementary Figs. 7–12, Supplementary Note 1, and Supplementary Table 1) PNPs acting as piezocatalysts with a size of <100 nm are sensitive to structural deformation induced by ultrasonic pressure, which facilitates charge separation and thus ensures high-efficient ROS generation (Fig. 1f, g)[22]. An NHS ester-based bioadhesive hydrogel, with a thickness of ~1 mm, was applied between the US array and the MN patch for optimal tissue-device integration. This hydrogel exhibits notable stretchability, and importantly, can form covalent amide bonds with interfaces (both transducer and skin), resulting in strong adhesion for continuous wearable US therapy (Fig. 1h and Supplementary Fig. 13)[13,23,24]. The US transducer incorporates a 4 × 6 matrix array of high-performance mKNN 1–3 piezoelectric composite units (2.5 mm × 2.5 mm × 1.5 mm) that are interconnected via island-bridge electrodes and encapsulated in biocompatible silicone elastomer, thereby achieving overall stretchability (Supplementary Figs. 14–16)[11,15]. We further quantified the strain on the transducer when stretched by 60% along the *x*-axis (Fig. 1i). Finite element analysis (FEA) results indicate a maximum tensile strain of ~1.5% in the copper interconnects (Fig. 1j). Overall, the MN patch, with its small size and thin backing film, can be fully covered and securely adhered to the skin by the larger bioadhesive hydrogel layer, ensuring reliable attachment of wf-UMP throughout the application (Supplementary Figs. 17 and 18).

The final transducer array is displayed in Fig. 1k, highlighting its flexibility and conformal contact on curved surfaces. The robust adhesion of the wf-UMP is shown in Fig. 1l, m and Supplementary Fig. 19, where it withstands high pulling forces (~5 N) and maintains seamless adhesion to skin, demonstrating its potential for application to non-planar surfaces. It also adheres well to skin under dynamic and sweaty exposures, enabling real-world applications (Supplementary Figs. 20 and 21 and Supplementary Movie 1). Furthermore, the effective penetration of the MNs into the mouse skin was validated by the hematoxylin and eosin (H&E) staining (Fig. 1n). In conclusion, wf-UMP demonstrates stable and robust adhesion to soft tissues, ensuring seamless contact even when coupled to complex surfaces, thus facilitating effective, painless drug delivery and sustained therapy (Supplementary Fig. 22).

Characterizations of wf-UMP

In the context of biosafety for wearable electronics, high-performance mKNN ceramics were selected as the functional material for electromechanical conversion of the transducer array (Supplementary Note 2), which were further processed into 1–3 piezo-units with a kerf of 200 μm and a pitch of 700 μm (Fig. 2a and Supplementary Fig. 23) to enhance the thickness electromechanical coupling coefficient (k_t) and

https://doi.org/10.1038/s41467-025-58075-z

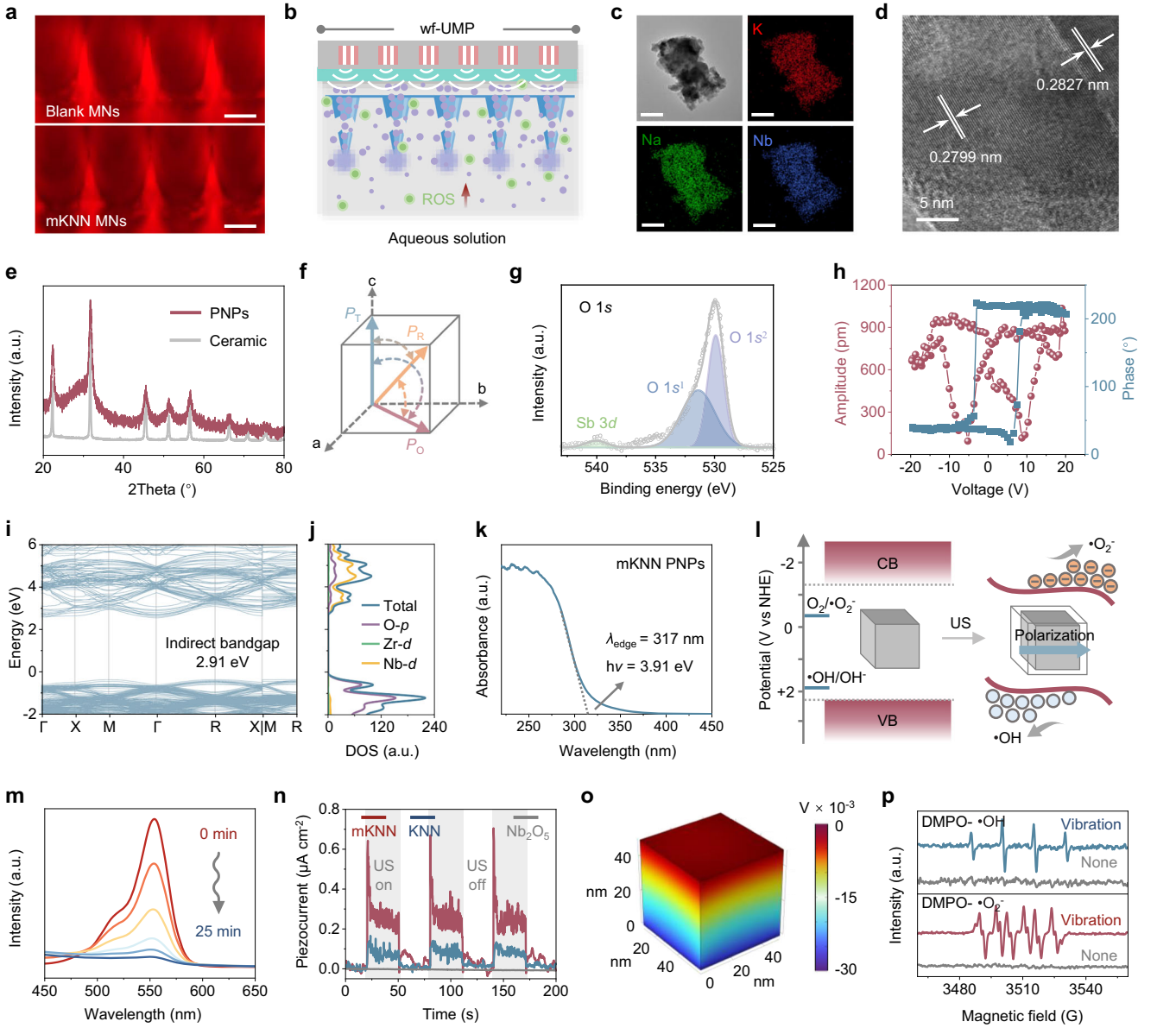

Fig. 3 | Mechanism, structural characterizations, and US-activated piezocatalysis of mKNN PNPs. a Fluorescence images of blank and mKNN MNs. mKNN MNs showed reduced fluorescence particularly at the tips. Scale bars, 600 μm. **b** Schematic illustration of US-activated piezocatalysis of mKNN PNPs loaded in dissolvable MNs. **c** TEM images and corresponding EDS mapping results of mKNN NPs. Scale bars, 100 nm. **d** HR-TEM image of mKNN PNPs. Scale bar, 5 nm. **e** XRD patterns of mKNN ceramic and PNPs. **f** The spontaneous polarization vectors of mKNN materials with R-O-T phase coexistence. **g** XPS spectra of O 1*s* for mKNN PNPs. **h** SS-PFM amplitude curve and phase loop of mKNN PNPs. **i**, **j** Electronic band structure (**i**) and density of states (**j**) of mKNN PNPs determined by DFT calculations. **k** UV-vis diffuse reflectance spectra of mKNN PNPs. **l**, Schematic illustration of electron and hole generation, transfer, and utilization in mKNN PNPs for piezocatalysis. **m** Degradation of Rho B by mKNN PNPs under US stimulation. **n** Piezocurrents of KNN, mKNN, and non- piezoelectric Nb_2O_5 PNPs under periodic US stimulation. **o** FEA simulation of surface piezo-potential distribution of a mKNN PNP under the acoustic pressure generated by wf-UMP. **p** EPR spectra of DMPO-$^{\cdot}$OH and DMPO-$^{\cdot}O_2^-$ over mKNN PNPs under US stimulation.

reduce acoustic impedance (Z_a)[11,25]. The efficiency of electro-mechanical conversion can be quantified by the resonance frequency (f_r) and antiresonance frequency (f_a) of the impedance spectra (Fig. 2b and Supplementary Fig. 24). Compared to the isotropic bulk ceramic, the anisotropic 1–3 piezo-unit exhibited higher k_t (~0.53) due to the suppression of the shear vibrating modes (Fig. 2c). Moreover, the lower Z_a (~10 MRayl) of 1–3 piezo-units further improved the acoustic coupling and thus acoustic transmission efficiency. Since the filled epoxy polymer is without ferroelectric polarization, the polarization and strain values of the 1–3 piezo-units were degraded (Supplementary Fig. 25); however, the well-preserved piezo/ferroelectricity still ensures stable electrical performance and US emission. Ultimately, the 1–3 piezoelectric transducer exhibits a center frequency of 1.2 MHz and a −6 dB bandwidth of 58% (Fig. 2d).

Furthermore, we assessed the electrical impedance of the device under deformation. The stable impedances of wf-UMP with increasing bending curvatures indicate that mechanical deformation has minimal influence on device performance (Fig. 2e). Tensile properties were evaluated by stretching experiments on wf-UMP along the *x*-axis from 0 to 80%, as visualized by piezo-units in a 2 × 2 array region (Supplementary Fig. 26). The serpentine interconnects unraveled, rotated, and twisted when loaded with tensile stresses, thereby relieving the strain on the electrode islands[11,26,27]. The wf-UMP can be reversibly stretched up to 60% in one direction. With further stretching up to 80%, plastic

deformation of the serpentine interconnect as well as partial delamination from the silicone elastomer can be observed upon release (Fig. 2f and Supplementary Fig. 26)[11,15]. These special geometrical and electrical designs enable wf-UMP to exhibit an elastic strain level of ~60% and an optimal operating frequency of 1.2 MHz. To assess the adhesion capability of wf-UMP, we performed the standard 180°-peeling test to quantify the interfacial toughness of the bioadhesive hydrogel on porcine skin (Fig. 2g). The interfacial toughness between the hydrogel and porcine skin is >500 J m^{-2}, demonstrating a robust adhesion of wf-UMP on soft tissues[23,28]. Under mechanical stresses such as bending and stretching, wf-UMP maintains stable adhesion without delamination or loss of contact (Supplementary Fig. 27). Moreover, the acoustic impedance of the bioadhesive hydrogel was experimentally measured to be ~1.54 MRayl, which is comparable to commercial US gels and skins (~1.5 MRayl) and ensures the efficiency of US transmission (Supplementary Fig. 28)[25].

We employed FEA to simulate the US beam pattern emitted by wf-UMP. Compared to the bulk ceramic unit exhibiting a spreading US field, US beams emitted by 1–3 piezo-unit show improved longitudinal directivity, magnitude, and penetration depth of >15 mm (Fig. 2h and Supplementary Figs. 29 and 30). In terms of wf-UMP, it demonstrates more converged beams with penetration depths up to ~100 mm, enabling efficient diffusion and activation of mKNN PNPs injected directly into the skin via the MN patch or into the body via subsequent systemic circulation (Fig. 2i). The larger the piezoelectric array, the greater the ultrasonic power and the deeper the penetration. The acoustic pressure generated by wf-UMP over the input voltage ranging from 10 Vpp (peak-to-peak voltage) to 120 Vpp was measured, which increased with input voltages and was higher than that of the device fabricated by mKNN ceramics (Fig. 2j and Supplementary Fig. 31). Regarding the safety assessment of acoustic exposures on human tissue, we calculated safety parameters of wf-UMP, including the spatial-peak temporal average (I_{SPTA}), the spatial-peak pulse average (I_{SPPA}), the mechanical index (MI), and the thermal index (TI) (Fig. 2k and Supplementary Fig. 32). All of these parameters are positively correlated with the input voltage, indicating that the acoustic output of wf-UMP can be flexibly adjusted to ensure safe operation (input voltage <70 Vpp, based on U.S. Food and Drug Administration (FDA) limits)[12,29,30]. Furthermore, the thermal effects of wf-UMP were evaluated by direct imaging with an infrared camera. The temperature of wf-UMP increased by 3.2 °C when the device was placed on an agarose hydrogel and operated at an input voltage of 20 Vpp for 30 min, indicating a negligible device thermal effect and thermal-induced drug diffusion (Fig. 2l and Supplementary Figs. 33 and 34)[31].

To reveal the drug delivery performance of wf-UMP, the device was adhered on the agarose hydrogel to visualize the release and diffusion behavior of the drug-loaded MN patch[32]. Notably, the MN patch demonstrated excellent solubility, ensuring rapid dissolution and drug release upon wf-UMP application (Supplementary Figs. 35 and 36 and Supplementary movie 2). To further investigate the effect of US stimulation, Rho B-labeled wf-UMP devices were pressed into agarose hydrogels and held in place for 2 min, during which one group of agarose hydrogels received US stimulation (US+) while the other served as a control without US stimulation (US-) (Supplementary Fig. 37). Cross-sectional images of hydrogels were recorded at different time points to track drug diffusion (Fig. 2m). The results demonstrated enhanced diffusion in the US+ samples, with a drug penetration depth of ~4.6 mm at 30 min, which was twice that observed in the control group (~2.3 mm). While these results highlight a trend of improved diffusion under US stimulation, it is important to note that agarose hydrogel serves only as a preliminary model for diffusion visualization and does not replicate the complex structural and mechanical properties of skin tissues. To further validate these findings, confocal microscopy was used to analyze the permeation depth of Rho B into porcine skin. wf-UMP devices were applied to porcine skin under identical conditions (pressed for 2 min), and the diffusion depth of Rho B was examined. At a depth of 328 µm, the US+ sample exhibited significantly higher fluorescence intensity compared to the control group (Fig. 2n). The total diffusion depth in the US+ samples reached ~500 µm, compared to <400 µm in the US- group (Supplementary Fig. 38). These results further confirm that US stimulation enhances the diffusion of Rho B into tissue, indicating the potential of wf-UMP for efficient transdermal drug delivery.

US-activated catalysis of mKNN PNPs

The distribution of mKNN PNPs within the MNs was observed to be relatively homogeneous, with slight clustering localized near the tip region (Fig. 3a). Upon application, the dissolvable mKNN MN portion in wf-UMP will rapidly dissolve in aqueous environments or tissues, releasing the mKNN PNPs, enabling them to be activated by US stimulation and exert their catalytic functionality (Fig. 3b). The optimized mKNN PNPs are irregularly shaped with a size of <100 nm and the contained elements are homogeneously distributed (Fig. 3c and Supplementary Fig. 39). High-resolution transmission electron microscope (HR-TEM) images showed clear and well-ordered lattice fringes extending throughout the mKNN crystals (Fig. 3d and Supplementary Fig. 40). The calculated interplanar spacings (d) of 0.2799 nm and 0.2827 nm belong to (101) lattice plane of tetragonal (T) phase and (111) of orthorhombic (O) phase, respectively. The selected-area electron diffraction (SAED) patterns also displayed distinct rings (Supplementary Fig. 41). Subsequently, the crystal structure of mKNN PNPs was evaluated by X-ray powder diffraction (XRD) pattern, which resembles the multiphase coexisting mKNN ceramic, as the lowered energy barrier will promote polarization rotation and thus enhance piezoelectricity (Fig. 3e, f). Notably, the diffraction peaks of mKNN PNPs were significantly weakened and widened due to the decrease in crystallinity and particle size[33,34]. The chemical nature of mKNN PNPs was investigated by XPS analysis, which revealed that oxygen vacancies could further enhance the piezocatalytic activity (Fig. 3g, Supplementary Fig. 42, and Supplementary note 3). The piezoelectricity of PNPs on the nanoscale was confirmed by switching spectroscopy PFM (SS-PFM). Both mKNN and KNN (abbreviation for unmodified $K_{0.48}Na_{0.52}NbO_3$-0.2% Fe_2O_3) PNPs demonstrated characteristic butterfly-shaped amplitude curves and rectangular phase loops (Fig. 3h and Supplementary Fig. 43). However, mKNN PNPs displayed higher amplitude (>900 pm) and phase contrast (~180°) compared to KNN PNPs (amplitude <300 pm, phase contrast ~120°) under an applied voltage of ±20 V, indicating favorable intrinsic piezorespone and complete domain switching in mKNN PNPs. Additionally, these PNPs were developed into piezoelectric energy harvesters (PEHs), and their electrical outputs were measured under mechanic force. Under identical instantaneous force impacts, the average open-circuit output voltage (~16 V) of the mKNN-based PEH was four folds higher than that of the KNN-based PEH (~4 V), further validating the enhanced piezoelectric properties of mKNN PNPs (Supplementary Fig. 44).

In view of the importance of energy band structure in piezocatalytic activities, we first employed density function theory (DFT) calculations to theoretically investigate the energy band structure of mKNN. The mKNN exhibits an indirect electronic band gap of 2.91 eV, where the valence band maximum (E_{VB}) originates from the O 2p orbital, while the conductive band minimum (E_{CB}) arises from the coupling of the O 2p and Nb 3d orbitals (Fig. 3i, j). The experimentally determined energy gap (E_g) of mKNN PNPs via UV-vis spectra was measured to be 3.91 eV (Fig. 3k, Supplementary Fig. 45, and Supplementary note 4), exceeding the calculated value. Generally, a decrease in particle size (especially at the nanometer size) would enhance the energy barrier among charge carriers, resulting in wider energy gaps[33,35].The mechanism of piezocatalysis is schematically illustrated in Fig. 3l. Periodic US stimulation induces the generation of a built-in piezo-potential field and energy band bending in mKNN PNPs, which

promotes continuous separation and transmission of charge carriers (for example, electrons and holes) and thus facilitates the surface redox reactions, ultimately leading to the production of ROS •OH and $\cdot O_2^-$[22,33].

Next, we assessed the piezocatalytic activity of mKNN PNPs through the degradation of Rho B. After 25 min of US stimulation, notable decreases in absorption peak intensity were observed, with a high degradation rate of $110 \times 10^{-3}\,min^{-1}$ (Fig. 3m, Supplementary Fig. 46, Supplementary note 5, and Supplementary table 2). Generation, separation and migration of electron-hole pairs are crucial factors determining the efficiency of piezocatalysis[4,36,37]. Therefore, we measured the transient piezoelectric currents of mKNN PNPs under periodic US stimulation (Fig. 3n). The results show prominent current peaks upon exposure to US stimulation, indicating effective separation and migration of charges. In contrast, non-piezoelectric Nb_2O_5 (raw material of mKNN and KNN) PNPs showed no response to US stimulation, further demonstrating that the charge separation and migration are induced by the piezoelectric effect. Moreover, the piezocurrents of mKNN PNPs were proportional to the US intensity (Supplementary Fig. 47). FEA findings reveal the surface piezopotential distribution of the mKNN PNP under the acoustic pressure generated by wf-UMP, which indicates the sufficient energy for charge carrier migration (Fig. 3o)[22]. Subsequently, electron paramagnetic resonance (EPR) spin-trapping experiments were carried out to detect the generated free radicals using 5, 5-dimethyl-1-pyrroline N-oxide (DMPO). Typical peaks corresponding to DMPO-•OH and DMPO-$\cdot O_2^-$ were observed under US stimulation, confirming the existence of ROS •OH and $\cdot O_2^-$ in the piezocatalytic process (Fig. 3p). Note that the mKNN PNPs remained structurally stable after US stimulation, highlights the negligible effect of US on the piezoelectric properties of mKNN PNPs and their continuous piezocatalytic applications (Supplementary Fig. 48).

In vitro anticancer activity of mKNN PNPs

We investigated the formation of cellular ROS to elucidate the mechanism of nontoxicity and biocompatibility mKNN PNPs as a piezocatalyst for anticancer treatment (Supplementary Fig. 49 and Supplementary note 6). The results indicated that the non-piezoelectric HA and Nb_2O_5 did not affect ROS production in cells. However, 4T1 cells treated with mKNN+US exhibited a substantial increase in intracellular ROS levels, as evidenced by higher green fluorescence and significant average fluorescence intensity (Fig. 4a, b and Supplementary Fig. 50). Therefore, the mKNN PNPs, possessing superior piezoelectric performance, enhance PCT to tumors primarily by increasing ROS production while minimize the impact on surrounding healthy cells. Flow cytometry (FCM) analysis of apoptosis confirmed a significantly higher apoptosis level in 4T1 cells treated with mKNN+US compared to those treated with mKNN only, whereas no significant increase in apoptosis levels was observed in the HA and Nb_2O_5 groups, regardless of US stimulation (Fig. 4c and Supplementary Fig. 51). Furthermore, JC-1 dyes were employed to investigate changes in mitochondrial membrane potential (MMP)[38], as excessive ROS production is associated with mitochondrial dysfunction. The mKNN+US group exhibited the most intense green fluorescence and weakened red fluorescence compared to the control groups, suggesting that mKNN +US significantly heightened oxidative stress and reduced MMP in 4T1 cells, which may account for the induced apoptosis (Fig. 4d, e and Supplementary Fig. 52). Similarly, treatment with mKNN+US in 4T1 cells significantly increases the ratio of dead to live cells compared to mKNN alone (Supplementary Fig. 53). Moreover, the number of migratory 4T1 cells treated with mKNN+US was markedly reduced (Fig. 4f and Supplementary Fig. 54). Consequently, intracellular ROS generated by mKNN PNPs under US stimulation effectively exert cytotoxic effects on 4T1 cells, inducing apoptosis and inhibiting cell migration.

In vivo anticancer activity of wf-UMP

Next, we carried out in vivo experiments using a 4T1 subcutaneous tumor model to investigate the capability of wf-UMP in inhibiting tumor growth (Supplementary Fig. 55). Figure 4g illustrates the treatment design of wf-UMP for early-stage tumors. It is evident that tumors were effectively suppressed in the wf-UMP group within 2 weeks, with negligible effects observed upon US stimulation and MN insertion (Fig. 4h and Supplementary Fig. 56). Specifically, the efficacy of wf-UMP in delaying and inhibiting tumor growth was superior to the other groups, which was further validated by the reduced weights and volumes of the resected tumors (Fig. 4i, h). The survival monitoring results of mice after treatment in each group showed that wf-UMP could effectively prolong the survival of mice (Fig. 4k). Notably, wf-UMP demonstrated effective antitumor therapeutic effects in a wearable and minimally invasive manner, with exceptional biosafety evidenced by minimal weight fluctuations and no significant toxic side effects observed in major organs (heart, liver, spleen, lung, and kidney) (Fig. 4l and Supplementary Fig. 57). Tumor sections stained with H&E demonstrated the therapeutic efficacy of wf-UMP, characterized by the largest areas of tumor necrosis (Fig. 4m). Immunofluorescence staining of Ki-67 revealed a significantly reduction in highly proliferative tumor cells following wf-UMP treatment (Fig. 4m, n), and TUNEL staining histological analysis further confirmed its enhanced therapeutic effect of inducing tumor cell apoptosis (Fig. 4m, o). Anti-CD31 antibody labeling of tumor vasculature showed the smallest red area in the wf-UMP group, indicating the suppression of tumor blood vessel proliferation (Fig. 4m, p). Collectively, wf-UMP effectively suppresses tumor cell growth and proliferation by mediating oxidative stress amplification, and offers a secure and efficient PCT approach for early-stage cancers.

In vivo biosafety of wf-UMP and metabolic distribution of mKNN PNPs

We further evaluated the biosafety of repeated use of the wf-UMP through in vivo experiments. Blank MN patches, mKNN MN patches, and wf-UMP were applied daily to mice for 5 consecutive days. Mild red traces of inflammation were observed at the application sites but resolved by day 10, with no significant skin damage detected during subsequent weekly applications (Fig. 5a). By day 10 and day 28, H&E staining of skin tissue revealed no significant differences in epidermal thickness between the wf-UMP group and the other treatment groups, confirming that no skin damage occurred during these treatments (Fig. 5b, c and Supplementary Fig. 58). Systemic biosafety was further assessed by examining primary organs, including the heart, liver, spleen, lungs, and kidneys, which showed no toxic side effects in any group (Fig. 5d). Hematological evaluations on day 28 indicated normal levels of white blood cells (WBC), red blood cells (RBC), and hemoglobin (HGB) across all groups (Fig. 5e–g). Additionally, blood biochemical analysis revealed no abnormalities in liver and kidney function markers, such as alanine aminotransferase (ALT), aspartate aminotransferase (AST), and creatinine (CREA), in the wf-UMP group compared to other groups (Fig. 5h–j). These results collectively confirm that wf-UMP exhibits excellent biosafety in in vivo cancer therapy.

The metabolism of mKNN PNPs at the treatment site was evaluated by measuring the concentration of Nb. Following wf-UMP application, Nb was detected in the subcutaneous tumor of mice, with its concentration gradually decreasing over time. Nevertheless, the mKNN PNPs remained localized at the treatment site throughout the treatment period, enabling sustained anti-tumor effect (Fig. 5k). To further investigate the distribution of mKNN PNPs after wf-UMP application, transmission electron microscopy (TEM) was employed to assess their localization in mouse subcutaneous tumors 4 h post-application. TEM images revealed that the mKNN PNPs were accumulated and randomly distributed throughout the tumor tissue and maintained their morphology (Fig. 5l).

https://doi.org/10.1038/s41467-025-58075-z

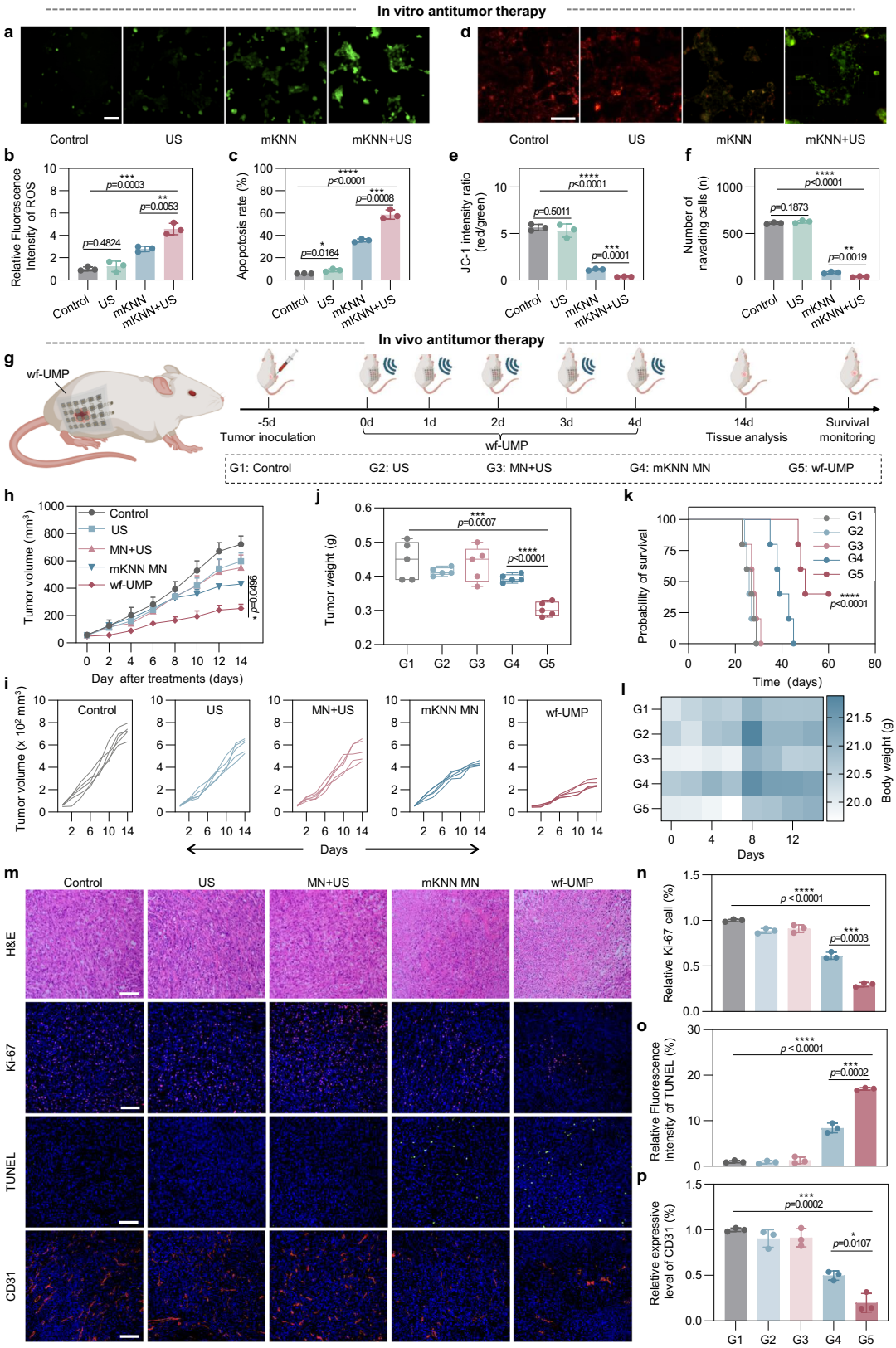

Immunomodulation of wf-UMP on tumor progression

To elucidate the underlying molecular mechanism between wf-UMP and its inhibition on breast cancer tumor growth, we conducted RNA sequencing analysis. A distinct pattern of gene expression was observed for the mKNN MN group without US activation (Supplementary Fig. 59). Upon comparison between the wf-UMP and control groups, we identified 467 differentially expressed genes (DEGs), comprising 248 down-regulated genes and 219 upregulated genes (Fig. 6a). Gene Ontology (GO) chord diagram analysis showed that the related genes regulated by wf-UMP were mainly involved in different gene groups related to immune processes (Fig. 6b). Further analysis using the Kyoto Encyclopedia of Genes and Genomes (KEGG) pathway

Fig. 4 | In vitro and in vivo antitumor effects of mKNN PNPs and wf-UMP. **a**, **b** Intracellular fluorescence images of ROS stained with DCFH-DA in 4T1 cells post various treatments (**a**) and corresponding quantification (**b**) ($n = 3$ independent samples). Scale bar, 100 μm. **c** Quantitative analysis of early and late apoptotic cell populations in each group ($n = 3$ independent samples). **d**, **e** Fluorescence images of 4T1 cells stained with JC−1 post-treatment (**d**) and the corresponding green/red fluorescence ratios (**e**) ($n = 3$ independent samples). Scale bar, 100 μm. **f**, Quantification of 4T1 tumor cell invasion capacity by Transwell assay following different treatments ($n = 3$ independent samples). **g**, Schematic diagram illustrating the application of wf-UMP to mouse and the treatment protocol. Created in BioRender. *Jin, J.* (2025) http://BioRender.com/x39n446. **h**, **i** Average (**h**) and individual (**i**) tumor growth curves for five groups of mice across distinct therapeutic regimens ($n = 5$ mice). **j** Comparative tumor weights of mice in each group on day 14 ($n = 5$ mice). Box plots show the median (center line), first and third quartiles (edges), and data range (whiskers). **k** Survival rate curves for tumor-bearing mice in each group ($n = 5$ mice). Statistical significance was estimated by the log-rank (Mantel–Cox) test with the mKNN MN group. **l** Body weights of mice in each group after 14 days of treatment (n = 5 mice). **m**, Histological analysis of tumors via H&E, Ki−67, TUNEL, and CD31 staining post-treatment ($n = 3$ independent samples). Scale bar, 100 μm. **n**–**p** Quantification of relative percentages of mean fluorescence intensity of Ki-67 positive cells (**n**), TUNEL (**o**), and CD31 (**p**) in each treatment group ($n = 3$ independent samples). Group annotations: G1, Control; G2, US; G3, MN + US; G4, mKNN MN; G5, wf-UMP. Results are presented as mean ± s.e.m. Statistical difference was calculated using a two-tailed unpaired student's *t*-test. Significance thresholds: $^{*}p < 0.05$, $^{**}p < 0.01$, $^{***}p < 0.001$, $^{****}p < 0.0001$. Source data are provided as a Source Data file.

enrichment analysis revealed the significant impact of wf-UMP on relevant signaling pathways, such as natural killer cell mediated cytotoxicity, T cell receptor signaling pathway, cytokine-cytokine receptor interaction, and NF-κB signaling pathway (Fig. 6c). Note that both cytokine-cytokine receptor interaction and T cell receptor signaling pathway exhibited a low *p*-value and a high enrichment index in the enrichment analysis, indicating their crucial role in wf-UMP-induced tumor regression (Fig. 6d, e).

Adaptive immunity, renowned for its persistence and specificity, represents a pivotal immune response capable of targeting perinecrotic tumor cells. To elucidate the mechanism by which wf-UMP modulates the tumor immune microenvironment, we collected 4T1 tumors 14 days after wf-UMP treatment and analyzed immunophenotypic changes using FCM analysis. The results showed that wf-UMP induced 8.50% $CD8^+$ cytotoxic T lymphocyte infiltration (gated by $CD3^+$ cells), surpassing that in other groups (Fig. 6f, g). Moreover, the FCM analysis confirmed elevated expression of $CD4^+$ T cells in tumors of the wf-UMP group (Fig. 6h). Compared to the other three groups, tumors treated with wf-UMP showed a reduction in myeloid-derived suppressor cells (MDSCs), along with a substantial increase in NKT cells (Fig. 6i–k). It is known that tumor-associated macrophages-M1 (TAM-M1) exhibit pro-inflammatory properties and potent effector activities against infections and cancer cells, whereas tumor-associated macrophages-M2 (TAM-M2) promote tumor cell development and metastasis[39]. The proportion of TAM-M1 and M1/M2 ratio in the tumors of 4T1 tumor-bearing mice was significantly higher in the wf-UMP group compared to the control group (Fig. 6l and Supplementary Fig. 60). Subsequently, serum samples from each group of mice were collected for enzyme-linked immunosorbent assay (ELISA) analysis to detect cytokine secretion levels, including interferon-γ (IFN-γ), interferon-β (IFN-β), interleukin-6 (IL-6), and tumor necrosis factor-α (TNF-α), aiming to further assess the antitumor immune response of wf-UMP. The results show that the secretion of IFN-γ, IFN-β, IL-6, and TNF-α induced by wf-UMP was 1.1, 1.18, 1.17, and 1.16-fold higher, respectively, compared to the mKNN MN group (Fig. 6m–p). Collectively, through the reactivation of immune cells and the enhancement of cytokine release, wf-UMP sustains and stimulates immune cell proliferation, contributing to antitumor therapy.

Abscopal effect of wf-UMP combined with PD1 blockade

Based on the immunological response induced by wf-UMP in the subcutaneous tumor model of 4T1 breast cancer mice, we further investigated the synergistic effect of wf-UMP and Anti-PD1 in inducing systemic antitumor immunity using a dual tumor model. Five days prior to treatment initiation, 1×10^6 4T1 cells were injected into the right side of the mice to construct primary tumor, and 5×10^5 4T1 cells were subcutaneously inoculated into the left side three days prior to treatment to establish a distal tumor model. Anti-PD1 was injected intraperitoneally on days 0, 2 and 4 to monitor the abscopal effect. The primary tumor was treated with wf-UMP for five consecutive days, while the contralateral tumor remained untreated (Fig. 7a). The results indicated a limited effect of Anti-PD1 on primary and distant tumors (Fig. 7b, c and Supplementary Fig. 61). Notably, while the Anti-PD1+mKNN MN treatment effectively inhibited primary tumor growth, the Anti-PD1+wf-UMP treatment exhibited notable antitumor efficacy, with complete eradication of primary tumors in three out of five cases (Supplementary Figs. 62 and 63). Furthermore, the Anti-PD1+wf-UMP group demonstrated significant efficacy in reducing untreated contralateral tumors (Fig. 7c, d). H&E-stained primary and distant tumors reveled substantial tumor damage, further indicating that synergistic immunotherapy can improve breast cancer outcomes (Supplementary Fig. 64). Moreover, there were no notable changes in body weight among the treated mice, and H&E staining of major organs revealed no significant toxic side effects across all treatment groups, indicating the safety and tolerability of synergistic immunotherapy (Supplementary Figs. 65 and 66). In view of the promising efficacy of Anti-PD1 combined wf-UMP immunotherapy in tumor suppression, we further conducted fluorescent staining of Ki-67, TUNEL, and CD31 for bilateral tumors. While Anti-PD1 treatment led to a modest decrease in Ki-67 staining and a limited number of TUNEL-positive cells due to antibody-mediated immunity, the incorporation of Anti-PD1 with wf-UMP resulted in a substantial reduction in Ki-67 staining and a higher percentage of TUNEL-positive cells, indicating significantly inhibited tumor cell proliferation and enhanced apoptosis in both primary and distant tumors. CD31 fluorescence staining also confirmed a notable reduction in angiogenesis in tumors subjected to Anti-PD1+wf-UMP treatment, further demonstrating the efficacy of synergistic immunotherapy with Anti-PD1+wf-UMP (Supplementary Fig. 64).

Synergistic immunotherapy-induced T cell-mediated antitumor immunity

To elucidate the therapeutic mechanism of wf-UMP combined with PD1 blockade, immune cells in primary and distant tumors were analyzed using FCM on day 14 post-treatment. The results showed that Anti-PD1+wf-UMP group exhibited strong immune activation and significantly improved maturity of DCs in the primary tumors, which was much higher than that of other treatment groups (Fig. 7e, f). As professional antigen-presenting cells (APCs), DCs play a critical role in activating T cells by presenting tumor antigens, and their maturation correlates with antigen presentation capacity[40]. As a result, the Anti-PD1+wf-UMP group exhibited a significant increase in $CD3^+$ T cells, $CD8^+$ T cells, and $CD4^+$ T cells in the primary tumors (Fig. 7g and Supplementary Figs. 67 and 68). For adaptive immunity, the percentage of intratumoral $CD8^+$ T cells in Anti-PD1+wf-UMP group was significantly higher than that of the other treatment groups in the distant tumors (Fig. 7h, i). In addition, CD69 was identified as an early marker of T cell activation, and the results showed that the proportion of $CD8^+CD69^+$ T cells in the distal tumors of the Anti-PD1+wf-UMP treatment group was much higher than other groups (Fig. 7j)[41]. This group also showed dramatic increases in TAMs-M1, M1/M2 ratio and

https://doi.org/10.1038/s41467-025-58075-z

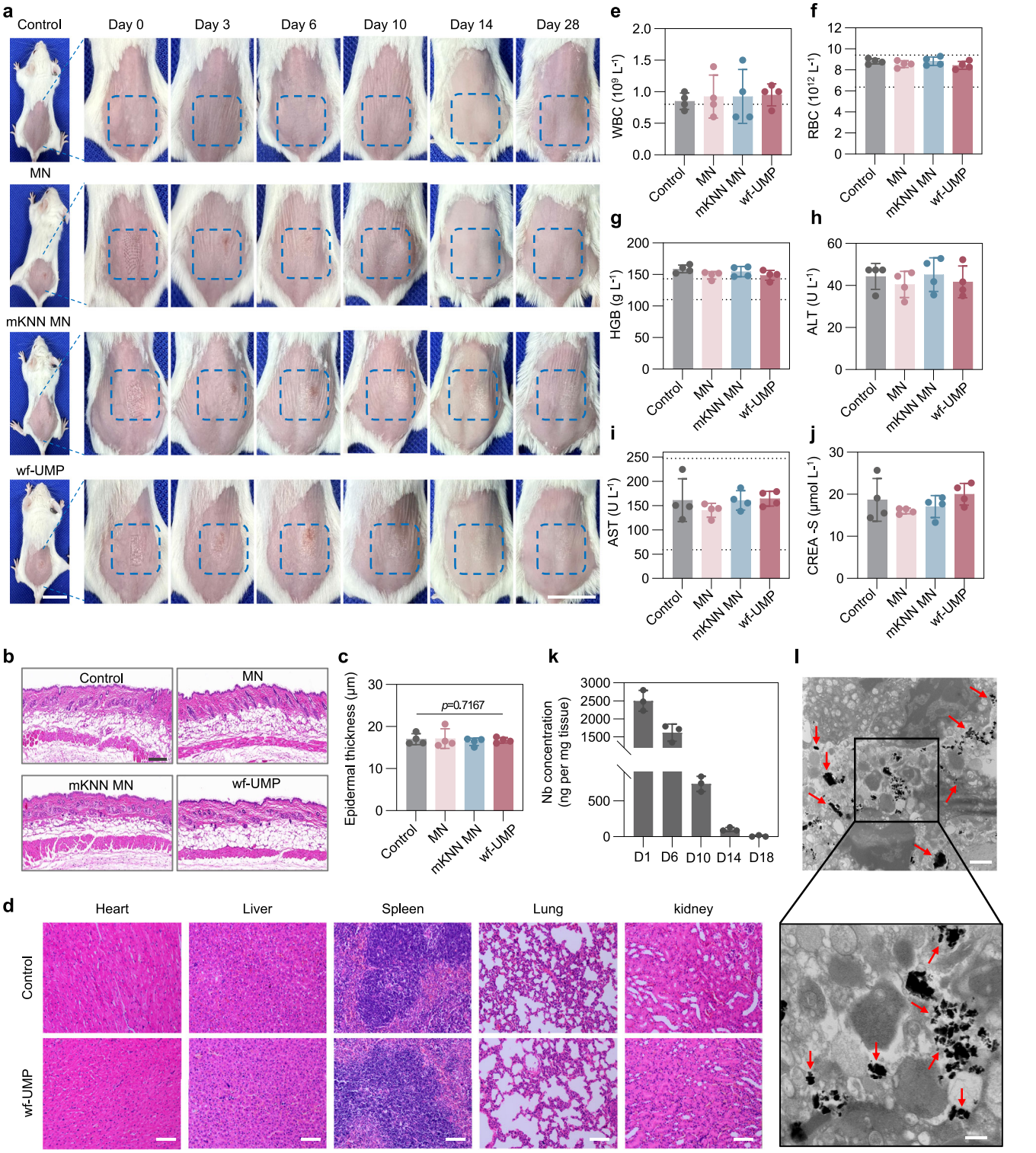

Fig. 5 | In vivo biosafety of wf-UMP and metabolic distribution of mKNN PNPs. **a** Representative images of skin condition at the treated site (blue dotted box) in healthy Balb/c mice at days 0, 3, 6, 10, 14, and 28 after treatment with blank MN patch (MN), mKNN MN patch (mKNN MN), and wf-UMP ($n = 4$ mice). Scale bars, 1 cm. **b**, **c** H&E staining (**b**) and epidermal thickness of the skin (**c**) in healthy Balb/c mice following various treatments on day 28 ($n = 4$ independent samples), while ns denotes no significance. Scale bar, 200 μm. **d**, H&E staining of major organs (heart, liver, spleen, lung, and kidney) from mice treated with control and wf-UMP at the experimental endpoint. Scale bars, 100 μm. **e**–**g** Blood routine test results for WBC (**e**), RBC (**f**), and HGB (**g**) in mice after treatments on day 28 ($n = 4$ biologically independent mice). **h**-**j**, Liver aminotransferase levels for ALF (**h**), AST (**i**), and creatinine (**j**) levels in the blood after different treatments detected on day 28 ($n = 4$ biologically independent mice). **k** Quantification of Nb concentration in tumors over time following wf-UMP treatment, measured by ICP-OES, showing the retention of mKNN PNPs at the tumor site (n = 3 independent samples). **l** Representative biological TEM images showing distribution of mKNN PNPs within tumors post-treatment with wf-UMP. Red arrows indicate clusters of nanoparticles. Scale bars, 2 μm (top) and 500 nm (bottom). All data are represented as mean ± .e.m. Statistical difference was calculated using a two-tailed unpaired student's *t*-test. Source data are provided as a Source Data file.

https://doi.org/10.1038/s41467-025-58075-z

NKT cells in distant tumors, while MDSCs and regulatory T cells (Tregs) were significantly decreased, compared to both PD-1 blockade alone and Anti-PD1+mKNN MN treatment groups (Fig. 7k-o and Supplementary Figs. 69 and 70). $CD8^+$ T cell infiltration in the tumor microenvironment (TME) is important for the efficacy of immune checkpoint inhibitors (ICIs). Previous studies have established a correlation between the frequency of $CD8^+$ T $PD\text{-}1^+$ cells in the TME and the clinical efficacy of PD-1 blockade therapy[42]. Furthermore, the depletion of $CD8^+$ T cells due to PD-1 overexpression is a key mechanism of immune evasion in tumors[43]. The results showed that the proportion of $CD8^+$ T $PD\text{-}1^+$ cells in the Anti-PD1+wf-UMP treatment group was significantly reduced compared to other control groups

Fig. 6 | Transcriptome and anti-tumor immune mechanism analysis of wf-UMP. **a** Volcano plots of DEGs between wf-UMP and control cohorts. Significant DEGs (red and blue dots): adjusted p-value < 0.05, fold change >2. **b** Gene ontology (GO) chord plot revealed that the regulation of immune-related genes in different clusters. **c** Enrichment study highlighting KEGG pathways relevant to immune function. **d**, **e** Gene set enrichment analysis-enriched pathways of cytokine-cytokine receptor interactions (**d**) and T cell receptor signaling pathways (**e**) in wf-UMP compared to control. **f** FCM results of $CD3^+CD8^+$ T cells and $CD3^+CD4^+$ T cells infiltrated in tumors. **g**, **h** Quantitative analysis of tumor-infiltrating $CD3^+CD8^+$ T cells (**g**) and $CD3^+CD4^+$ T cells (**h**) ($n = 3$ independent samples). **i** Representative flow cytometric analysis of MDSCs. **j-l**, Relative quantification of MDSCs (**j**), NKT cells (**k**), and TAM-M1 (**l**) ($n = 3$ independent samples). **m**–**p** Quantification of IFN-γ (**m**), IFN-β (**n**), IL-6 (**o**), and TNF-α (**p**) across treatment groups ($n = 3$ independent samples). All data are represented as mean ± s.e.m. Statistical difference was calculated using a two-tailed unpaired student's t-test. Significance thresholds: $^*p < 0.05$, $^{**}p < 0.01$, $^{***}p < 0.001$, $^{****}p < 0.0001$. Source data are provided as a Source Data file.

(Fig. 7p). Moreover, serum cytokine assays (including IFN-γ, IL-6, IL-12P70, and TNF-α) revealed that Anti-PD1+wf-UMP treatment induced markedly higher cytokine secretion compared to all other groups (Fig. 7q–t).

To facilitate immunosuppression, monocytes derived from the enlarged spleen migrate to the TME[44]. The spleen weights in the control and US groups were significantly higher compared to the other groups, whereas the Anti-PD1 and Anti-PD1+mKNN MN groups exhibited a slight reduction in spleen weights. Notably, spleens in the Anti-PD1+wf-UMP group showed normal morphology alongside significantly reduced weight compared to the other groups (Supplementary Fig. 71). These results suggest that synergistic immunotherapy attenuates splenomegaly and diminishes immunosuppression. Further, the synergistic immunotherapy was examined through FCM analysis to determine its capability to promote the expansion and proliferation of cytotoxic T lymphocytes in peripheral immune organs, aiming to elucidate the mechanism of interaction between Anti-PD1 and wf-UMP in enhancing antitumor efficacy. Evaluation of immune cells in the spleen reveled a significant increase in tumor-infiltrating T cells ($CD3^+CD8^+$) in the Anti-PD1+wf-UMP group with a suppression of MDSCs (Fig. 7u, v and Supplementary Fig. 72). These findings indicate that this synergistic immunotherapy poses a great potential in activating immune responses, thereby effectively promoting the activation of cytotoxic T lymphocyte and down-regulating immunosuppressive cells.

Furthermore, polychromatic immunofluorescent staining of primary and distant tumors showed that Anti-PD1+wf-UMP treatment resulted in increased $CD8^+$ and $CD4^+$ staining in both tumors, which is essential for inducing cytotoxic T cell-mediated immunotherapy. Conversely, staining for Forkhead box P3-positive (Foxp3), a marker indicative of Tregs, notably decreased (Fig. 7w and Supplementary Fig. 73). Moreover, there was a significant increase in $F4/80^+$ and $CD86^+$ staining following treatment with Anti-PD1+wf-UMP, indicating an increase in M1 macrophages in both primary and distant tumors (Supplementary Fig. 74).

Long-term immune memory function

Immune memory response is critical for tumor prevention and recurrence. To assess the immune memory effect of Anti-PD1+wf-UMP treatment, we performed a tumor rechallenge study. Tumors were reinoculated on the left side of the mice at day 30 after the end of combination therapy, and controls were sex- and age-matched mice that had not been previously inoculated with tumors (Fig. 8a). The results showed that the Anti-PD1+wf-UMP group effectively inhibited the growth of reinoculated distant tumors, whereas the tumors of the control mice progressed rapidly, which was also confirmed by tumor weights (Fig. 8b–f and Supplementary Fig. 75). To further investigate the long-term antitumor immune memory induced by the Anti-PD1+wf-UMP treatment, we analyzed the expression of antigen-specific memory T cells in the spleen, including effector memory T (Tem) cells ($CD44^+$ $CD62L^-$) and central memory T cells (Tcm) cells ($CD44^+$ $CD62L^+$). Tem subsets, which are localized in peripheral tissues, provide rapid responses to antigen exposure and immediate protection through the production of multiple cytokines[39]. FCM results showed that the Anti-PD1+wf-UMP treatment elicited a sustained antitumor response compared to other groups, characterized by a significant transition from the Tcm to the Tem phenotype. Specifically, this treatment upregulated Tem ($CD44^+$ $CD62L^-$) and down-regulated Tcm ($CD44^+$ $CD62L^+$) in both $CD8^+$ and $CD4^+$ T cells (Fig. 8g–i). These findings indicate that Anti-PD1 combined with wf-UMP not only induces specific long-term protection but also effectively prevents tumor recurrence. Therefore, this combination immunotherapy inhibits systemic tumor formation and recurrence over an extended period. Collectively, Anti-PD1+wf-UMP presents a promising PCT strategy that improves antitumor immunity by further activating DCs maturation through ICD and the up-regulation of macrophage M1 phenotype polarization, thereby eliciting T cell-mediated anti-tumor immunity and effectively inhibiting tumor recurrence (Fig. 8j).

Discussion

We presented a principled design approach and implementation of an integrated wf-UMP for convenient, efficient, and minimally invasive cancer therapy based on a ROS-driven dynamic therapeutic strategy. By systematically optimizing materials and device architecture, the wf-UMP ensures to be robustly worn on curved and dynamic tissue surfaces for easy and effective manipulation in view of the soft mechanical properties and superior acoustic-electrical transduction characteristics, thereby efficiently generate ROS with optimized PNPs. Preclinical studies in mice have shown that wf-UMP is effective not only in treating localized cancers and modulating immunity, but also in inducing a synergistic immune response through the DCs maturation activated by ICD and the modulation of macrophage polarization in combination with Anti-PD1, thereby capable of targeting distantly located cancers and inhibiting tumor recurrence. Our study offers an approach to cancer immunotherapy and underscores the promise of clinical translation of such a wearable, portable platform. Furthermore, wf-UMP promotes the transformation towards preventive and proactive health care, enhancing accessibility and affordability of cancer therapy.

Considering the rapid advancements in wearable medical systems and the urgent need for personalized healthcare, the future integration of modules such as modulus, temperature, pH, and tissue oxygenation detections into wf-UMP could enable close-loop real-time monitoring and targeted therapy via artificial intelligence networks, contributing to the progression beyond current one-size-fits-all healthcare models[45]. For future iterative optimization, it is possible to implement a 2D phased array as the wearable ultrasonic probe to take full advantage of the deep penetration and directionality of US, which not only allows for zoned stimulation of tumors by beamforming technology without disturbing other healthy tissues, but also allows for continuous tracking of tumor status as well as physiological signals from deeper tissues before and after therapy by through clinical-quality US imaging[13,19,24,46]. The bioadhesive hydrogel can be further integrated with electrical, thermal, optical, and biological functions to facilitate the human-machine interaction of the device[47,48]. Biologically and genetically engineered PNPs are advised to interface with in vivo microbial system and enhance the bioavailability of loaded nanomedicines[49,50]. Moreover, leveraging the benefits of wf-UMP, the loaded nanomedicines can be functionalized and customized to target

https://doi.org/10.1038/s41467-025-58075-z

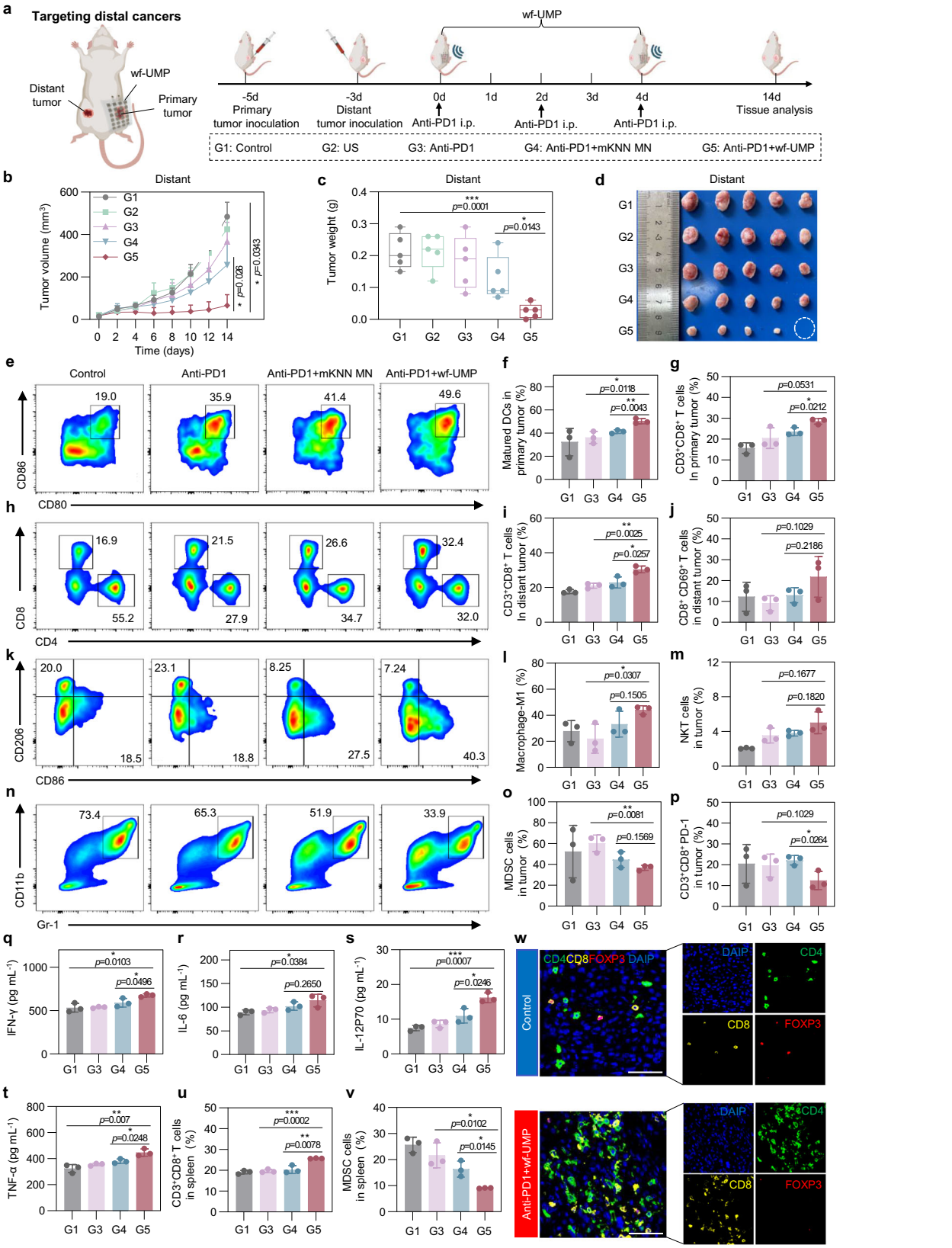

and treat various diseases, whether they present superficially on the skin or infiltrate deeper into tissues.

Given the complex physiological environment of living organisms, wf-UMP may demonstrate significant differences in therapeutic behavior and efficacy. Therefore, more in-depth studies into the immune reaction and immunosuppressive microenvironment are necessary to evaluate these therapeutic formulations and develop optimized strategies for cancer immunotherapy. For clinical translation, the realization of scalable and reproducible wf-UMP-based therapies that meet high standards may be challenging and require additional efforts. Further studies involving large animal models, clinical trials, and patient feedback are essential for advancements

Fig. 7 | Distal effects of wf-UMP induced synergistic immunotherapy and T cell-mediated anti-tumor immunity. a Schematic illustration of bilateral tumor treatment strategies. Created in BioRender. *Jin, J.* (2025) http://BioRender.com/x39n446. **b** Average tumor growth curves for distant tumors ($n = 5$ independent samples). **c** Tumor weights of distant tumors after various treatments ($n = 5$ independent samples). Box plots show the median (center line), first and third quartiles (edges), and data range (whiskers). **d** Gross images of distal tumors in each group (n = 5 independent samples). **e**, **f** Representative FCM analysis (**e**) and quantification of matured DCs (**f**) in primary tumors after different treatments (n = 3 independent samples). **g** Quantification of $CD8^+$ T cells in primary tumors (n = 3 independent samples). **h**, **i** Representative FCM analysis (**h**) and quantification (**i**) of $CD8^+$ T cells in distant tumor (n = 3 independent samples). **j** Relative quantification of $CD8^+CD69^+$ T cells in distant tumors following different treatments (n = 3 independent samples). **k**, **l** Representative FCM plots (**k**) and relative quantification (**l**) of macrophage-M1 in distant tumors ($n = 3$ independent samples). **m** Quantification of NKT cells in distant tumors ($n = 3$ independent samples). **n**, **o** Representative FCM plots (**n**) and quantification (**o**) of MDSCs in distant tumors ($n = 3$ independent samples). **p**, Quantification of tumor-infiltrating $CD8^+PD{-}1^+$ T cells in distant tumors ($n = 3$ independent samples). **q**–**t** Quantification of IFN-γ (**q**), IL-6 (**r**), IL-12P70 (**s**), and TNF-α (**t**) levels in different groups ($n = 3$ independent samples). **u**, **v** Relative quantification of $CD8^+$ T cells (**u**) and MDSCs (**v**) in the spleen ($n = 3$ independent samples). **w** Multicolor immunostaining images of distant tumors showing $CD4^+$, $CD8^+$, $Foxp3^+$, and DAPI cells in the control and Anti-PD1+wf-UMP groups. Scale bars, 50 μm. Group annotations: G1, Control; G2, US; G3, Anti-PD1; G4, Anti-PD1-PD1+ mKNN MN; G5, Anti-PD1+wf-UMP. All data are presented as mean ± s.e.m. Statistical difference was calculated using a two-tailed unpaired student's *t*-test. Significance thresholds: $^*p < 0.05$, $^{**}p < 0.01$, $^{***}p < 0.001$, $^{****}p < 0.0001$. Source data are provided as a Source Data file.

towards clinical applications. Meanwhile, establishing a clear regulatory pathway for wearable US electronics and setting standards for PCT will accelerate their safe and effective integration into clinical validation and potential FDA regulatory approval, ultimately transforming wf-UMP from a highly promising prototype to an indispensable instrument for personalized medicine[46].

Methods

Preparation of piezoceramics and corresponding PNPs

The piezoceramics of $0.95K_{0.48}Na_{0.52}Nb_{0.97}Sb_{0.03}O_3$-$0.05Bi_{0.5}Na_{0.5}ZrO_3$-0.2% Fe_2O_3 (abbreviated as mKNN) and $K_{0.48}Na_{0.52}NbO_3$-0.2% Fe_2O_3 (abbreviated as KNN) were synthesized using the conventional solid-state reaction method. High-purity raw materials including K_2CO_3 (99.0%), Na_2CO_3 (99.8%), Nb_2O_5 (99.5%), Sb_2O_3 (99.99%), Bi_2O_3 (99.99%), ZrO_2 (99.0%), and Fe_2O_3 (99.0%) purchased from Sinopharm Chemical Reagent Co., Ltd were accurately weighted according to their stoichiometric ratios, respectively. Then, the raw materials were ball-milled with alcohol and ZrO_2 balls for 24 h, followed by calcination at 850 °C for 6 h. Subsequently, the calcined ceramic powders were blended with 8 wt.% polyvinyl (PVA, Sinopharm Chemical Reagent Co., Ltd) and compressed into ceramic pellets under a pressure of 10 MPa. After the PVA was burned off, the ceramics were obtained by sintering the pellets at 1085 °C (mKNN) and 1090 °C (KNN) for 3 h. The poling process was carried out at room temperature with a direct current electric field of 2 kV mm^{-1}. For the piezocatalytic PNPs, the as-calcined powders were secondary ball-milled and then sand-grounded (VB-0.3Q, Suzhou Vgreen Nano-chem Technology Co., Ltd, China) at 2000 rpm for 8 h. The control material of Nb_2O_5 NPs was fabricated by directly sand-grounding the raw material Nb_2O_5.

Preparation of MN patches

For the MN patches, 300 mg of hyaluronic acid (HA, 10 kDa, Meilunbio, Dalian, China) were dissolved into 4 mL deionized water. 500 μL of the homogeneous solution were then dropped onto the polydimethylsiloxane (PDMS, Sylgard 184) MN mold. After keeping in a vacuum oven of 0.08 MPa for 10 min to remove bubbles, the MN mold fulfilled with HA solution was dried at 37 °C for 12 h. The MN patch was obtained by gently peeling it off from the mold (Supplementary Fig. 1). HA MN patches with chemical loadings were prepared by the same process, with 20 mg sufficient chemicals (mKNN PNPs) added at the beginning. To prepare the Rho B MN patches, 300 mg of HA were dissolved into 4 mL 1 mg mL^{-1} Rho B solution. The subsequent preparation process was similar to that of the HA MN patch mentioned above.

Preparation of polyacrylamide bioadhesive hydrogel and agarose hydrogel

First, 2 g of gelatin (Sinopharm Chemical Reagent Co., Ltd) and 6 mL of acrylic acid (AR, ChengDu Chron Chemicals Co., Ltd) were dissolved in 14 mL of deionized water. Subsequently, the photoinitiator α-ketoglutaric acid (0.04 g, 98%, Macklin), the cross-linker N,N'-methylenebisacrylamide (0.01 g mL^{-1}, 98%, Adamas-beta) and N-hydroxysuccinimide (NHS, 1% w/w, 98%, Tianjin Kemiou Chemical Reagent Co., Ltd) were added to the solution. After stirring for 10 min, the mixture was subjected to US to remove air bubbles. The bioadhesive hydrogel was then obtained by curing in silicon molds with an ultraviolet light (UV) chamber (284 nm, 10 W). Prior to use, the bioadhesive hydrogel was sealed in plastic bags and stored at −20 °C. The agarose hydrogel was fabricated by adding 2 g of agarose into 40 ml of deionized water and stirring for 30 min in a 100 °C oil bath. The solution was promptly poured into silicon molds and maintained at 4 °C until the agarose hydrogel was obtained.

Fabrication of wf-UMP

The detailed process of wf-UMP fabrication was shown in Supplementary Fig. 1. To optimize the performance of piezo-element, mKNN ceramics were initially processed into ceramic/epoxy (ELINOPTO E106-7 A/B) 1–3 composites via the dice-and-fill method (DS9260). Specifically, the ceramic pillars were designed with a width of 500 μm and a spacing of 200 μm. After being polished to the desired thickness, the 1–3 piezo-units were sputtered with Au electrodes on both sides (TPR450). Then the composites were cut into 2.5 mm × 2.5 mm × 1.5 mm cubes and poled. The 24 poled piezo-units were then neatly arranged and connected to the laser-cut island-bridge Cu/PI electrodes through silver paste (E-Solder 3022). The entire transducer array was subsequently encapsulated in silicon (Ecoflex 00–30) to ensure the flexibility and stretchability. Finally, the bioadhesive hydrogel and mKNN MN patch were implanted onto the surface of the encapsulated transducer array to form the device, wf-UMP.

Fabrication of PNPs-based PEHs

The PEH was manufactured by mixing PDMS, curing agent and mKNN/KNN PNPs in a weight ratio of 10:1:4. The resulting homogenous slurry was then spin-coated onto quartz glass. After drying at 80 °C for 4 h, the PDMS-mKNN/KNN films were peeled from the glass substrate. Subsequently, the films were cut into 2 cm × 2 cm squares and packaged with Cu/PI electrodes and Kapton films to create the PEHs.

Structure and performance characterization of mKNN and MN patch

The microstructure of MN patches was characterized by scanning electron microscope (SEM, agellan400, FEI Company) and optical microscope (SZM7045, SOPTOP). The distribution of mKNN PNPs within the MNs was further observed by inverted fluorescence microscope using Rho B as a marker. The permeation of the loaded drugs at different skin depths was characterized by confocal laser microscopy (Nikon A1si). The morphology, lattice fringes, and corresponding energy dispersive spectrometer were obtained by the high-

https://doi.org/10.1038/s41467-025-58075-z

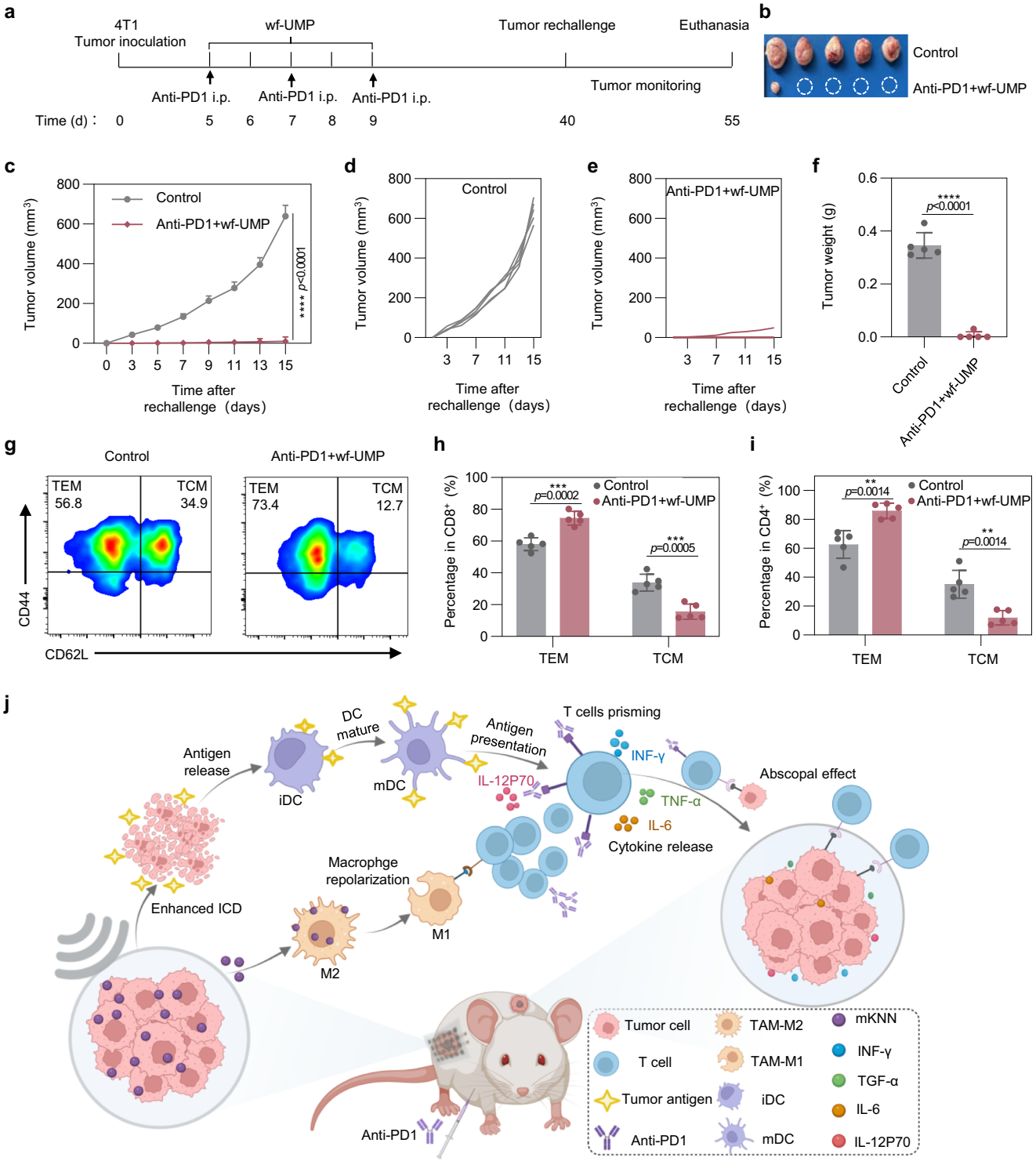

Fig. 8 | Long-term immuno-memory effects of wf-UMP in combination with PD1 blocker. a Schematic of the experiment timeline for the tumor rechallenge study. **b** Representative tumor images captured 15 days after tumor rechallenge ($n = 5$ independent samples). **c**–**e** Tumor growth curves during the rechallenge study: overall growth curves (**c**), individual tumor growth curves in the control group (**d**), and the Anti PD1+wf-UMP group (**e**). Data are presented as mean ± SD ($n = 5$ independent samples). **f** Tumor weights measured 15 days post-rechallenge ($n = 5$ independent samples). **g**, **h** Representative flow cytometric analysis (**g**) and quantification of effector memory T cell (Tem, $CD44^+ CD62L^-$) and central memory T cell (Tcm, $CD62L^+ CD44^+$) from $CD8^+$ T cells (**h**) in the spleen after different treatments ($n = 5$ independent samples). **i** Quantitative analysis of Tem and Tcm subsets from $CD4^+$ T cells in the spleen after different treatments ($n = 5$ independent samples). **j** Proposed mechanism of wf-UMP synergistic checkpoint blockade immunotherapy for distant tumor suppression. TAM-M1, tumor-associated macrophages-M1; TAM-M2, tumor-associated macrophages-M2; iDC, immature dendritic cells; mDC, mature dendritic cells. Created in BioRender. *Jin, J.* (2025) http://BioRender.com/r08a561. All data are presented as mean ± s.e.m. Two-sided Student's *t*-test was used to calculate the statistical difference between two groups. Significance thresholds: $^*p < 0.05$, $^{**}p < 0.01$, $^{***}p < 0.001$, $^{****}p < 0.0001$. Source data are provided as a Source Data file.

resolution transmission electron microscopy (HR-TEM, Thermo Scientific Talos F200X). To investigate the phase structure, both bulk ceramics and PNPs were assessed by XRD with Cu *K*α radiation (Bruker D8 Advanced XRD, Bruker AXS Inc., Madison, WI, USA). In addition, the temperature-dependent dielectric constants of bulk ceramics were investigated by the Dielectric Spectroscopy test system (TZDM-200-300, Harbin Julang Technology Co. Ltd., Harbin China) at elevating frequencies from 1 kHz to 100 kHz. PFM measurements were recorded by the piezoelectric force microscopy (PFM, MFP-3D, Asylum Research, Goleta, CA) with Dual AC Resonance-Tracking and SS-PFM modes. The *P-E* loops and *S-E* curves were characterized using a ferroelectric equipment (TF Analyzer 2000: aixACCT, Aachen, Germany) at 1 Hz. The surface chemical nature and valence band of PNPs were detected by the X-ray photoelectron spectroscopy (XPS, AXIS Ultra DLD). The bandwidth of PNPs was examined using the UV-vis spectrophotometer (UV-3600, Hitachi, Japan).

Performance of mKNN PNPs under US stimulation

To evaluate the piezocatalytic activity of mKNN PNPs, degradation experiments of Rho B under US stimulation (40 kHz, 120 W) were carried out. Specifically, 100 mg mKNN PNPs were added into 50 ml Rho B solution (5 mg L^{-1}). Note that the degradation experiments were carried out in darkness and the ambient temperature was preciously controlled within ± 1 °C to avoid photocatalysis and pyroelectric catalysis. The mixture was stirred in darkness for 30 min to reach adsorption-desorption equilibrium. Then, 3 mL of the mixture was pipetted and centrifuged every 5 min, and the supernatant from each centrifuged sample was further examined by a UV-vis spectrophotometer to determine the dye concentration.

The output voltages of the PNPs-based PEHs under instantaneous compression were recorded using an electrometer (6517B, Keithley). Transient piezo-currents of PNPs were tested by an electrochemical workstation (CHI660E, Shanghai Chenhua Instrument Corporation, China) equipped with a three-electrode system. Platinum served as the counter electrode, Ag/AgCl as the reference electrode, and FTO glass coated with PNPs functioned as the working electrode. The experiments were conducted in a 0.1 M Na_2SO_4 electrolyte solution. Then, the generation of ROS was detected by EPR (Bruker EMXplus X-Band EPR spectrometer) experiments after 5 min of US stimulation.

Characterization of wf-UMP

The impedances and phase angles of bulk ceramic, 1–3 piezo-unit, and wf-UMP were evaluated by an impedance analyzer (E4991B, Keysight, USA). The k_t and k_{eff} values can be calculated through the following Eqs. 1 and 2[11]:

$$k_t = \sqrt{\frac{\pi f_r}{2 f_a} \tan\left(\frac{\pi f_a - f_r}{2 f_r}\right)} \quad (1)$$

$$k_{eff} = \sqrt{1 - \frac{f_r^2}{f_a^2}} \quad (2)$$

The acoustic pressure of wf-UMP was measured by a hydrophone (3646, Precision Acoustics Ltd, UK). Thermal imaging pictures of wf-UMP in operation were recorded by a thermal imaging camera (H21Pro, Hikmicro).

Mechanical tests

The mechanical properties of MN patches were measured by the electronic universal testing machine (TSC504B), operating at a compression speed of 1 mm min^{-1}. For bioadhesive hydrogels, mechanical characterizations were conducted using an electronic universal testing machine (Instron 5967). Rectangular hydrogel samples, measuring 60 mm in length, 20 mm in width, and 1.6 mm in thickness, were evaluated at a constant tensile speed of 50 mm min^{-1}. To assess the adhesion performance of the bioadhesive hydrogel on porcine skin, 180° peeling tests were performed. Adhesion samples with an adhesion area measuring 2 cm in width and 6 cm in length were prepared and tested at a constant speed of 25 mm min^{-1}.

FEA simulations

FEA simulations on the mechanical performances, the acoustic outputs of wf-UMP, and the piezo-potential distribution of mKNN PNPs were conducted using COMSOL Multiphysics 6.1, ensuring strict adherence to the experiment settings. The physical parameters involved have been carefully considered and appropriately selected.

Theoretical calculations

First-principles calculations of the electronic properties of mKNN were conducted using the Vienna Ab initio Simulation Package (VASP) within the framework of density functional theory (DFT). To describe the exchange-correlation functional, the PBEsol parametrization of the generalized gradient approximation was employed. The wave functions were expanded in a plane wave basis set with a cut-off energy of 520 eV. For Brillouin zone sampling, Γ-centered *k*-point meshes with a grid of spacing 0.04 × 2π $Å^{-1}$ were utilized. The self-consistency cycle was iterated until achieving an energy convergence of 10^{-5} eV, the Kohn-Sham orbitals were updated.

Cells and animals

The 4T1 mouse breast cancer cell line (Cat CRL-2539) was sourced from the American Type Culture Collection (ATCC, Manassas, VA), while Hacat cells were obtained from the Laboratory of Radiation Medicine, School of Basic Medical Sciences, Sichuan University. 4T1 cells were cultured in RPMI Medium 1640 basic, and Hacat cells were maintained in Dulbecco's Modified Eagle's Medium (DMEM) supplemented with 10% fetal bovine serum (FBS, Gibcom, USA) and 1% penicillin/streptomycin (w/v). Cells were cultured in a humidified incubator at 37 °C with 5% CO_2. 6–8 weeks old Balb/c mice (female) were purchased from GemPharmatech LLC (Jiangsu, China) and housed in an environment with a 12 h light-dark cycle, an ambient temperature of 18-22 °C, and 50 - 60 humidity. All animal experiments were approved by the Animal Care and Use Committee of Sichuan University and conformed to the Guide for the Care and Use of Laboratory Animals published by the National Institutes of Health.

Cytotoxicity measurement

The cytotoxicity of mKNN against Hacat cells was evaluated using a CCK8 assay. Hacat cells were cultured at a density of 5×10^3 cells per well in 96-well plates and incubated overnight. Next, various concentrations of mKNN (0, 0.1, 0.2, 0.3, 0.4, and 0.5 mg mL^{-1}) were added to cell-containing medium for an additional 24 h. Finally, the standard CCK8 assay protocol was performed, and the optical density (OD) at 450 nm per null was detected using a microplate reader. The in vitro antitumor efficacy of mKNN against 4T1 cells was evaluated by CCK8 assay. In 96-well plates, 4T1 cells were cultured at a density of 5×10^3 cells per well. After 24 h of culture, mKNN at varying concentrations (0, 0.025, 0.05, 0.1,0.2, and 0.3 mg mL^{-1}) was added to 4T1 cells and co-cultivated for 4 h, followed by US stimulation (1.2 MHz, 30 s). Cells were stained with CCK8 solution and assessed using a microplate reader after an additional 24 h of incubation. Each experiment was performed independently three times.

ROS measurement

To assess intracellular ROS levels, 4T1 cells were inoculated into 6-well plates at a density of 2×10^5 cells per well and cultured for 24 h in fresh medium containing PBS, HA, Nb_2O_5, and mKNN at a concentration of 0.2 mg mL^{-1}. After 4 h of incubation, US stimulation (1.2 MHz, 30 s) was

applied. The cells were then labeled with DCFH-DA and observed using a fluorescence photographic recording.

Apoptosis assay

4T1 apoptosis was assessed as follows: 4T1 cells were inoculated into 6-well plates at 1×10^5 cells per well and cultured overnight. Cells were divided into 8 treatment groups: (1) PBS (control), (2) HA, (3) Nb_2O_5, (4) mKNN, (5) US, (6) HA + US, (7) Nb_2O_5 + US, and (8) mKNN+US. Cells in each group were treated for 4 h with the same concentrations of HA, Nb_2O_5 and mKNN, then stimulated with US (1.2 MHz, 30 s). After a further 24 h of incubation, the cells were stained with FITC-Annexin V/propidium iodide (PI) apoptosis detection kit and analyzed by FCM.

Live/dead cell staining and JC-1 staining

4T1 cells were seeded overnight in 6-well plates and divided into 4 groups: (1) PBS (control), (2) US, (3) mKNN, and (4) mKNN + US. After exposing the cells to the respective treatments for 4 h, the cells were stimulated with US for 30 s (1.2 MHz). Following cell staining with calcein-AM/PI and JC-1, the cells were incubated at 37 °C with 5% CO_2 for 30 min in a humidified environment. Subsequently, the cells underwent three PBS washes and were analyzed with a fluorescent microscope.

Transwell assay

To assess the impact of mKNN on cell migration, a transwell assay was conducted using the same treatment grouping and workflow as in the live/dead experiments. After US stimulation (1.2 MHz, 30 s), cells were collected, and 8×10^4 cells per well were seeded into the upper chamber with FBS-free 1640 medium, and the lower chamber, which contained medium supplemented with 10% FBS. Following a 24 incubation, cells that had migrated to the bottom of the polycarbonate membrane were fixed with 4% paraformaldehyde and stained with 0.1% crystal violet. The migration of cells was then recorded using a fluorescence microscope.

In vivo tumor therapy

Female Balb/c mice were acclimatized to the environment for 1 week before tumor model induction. Unilateral tumor model was established by subcutaneous injection of ~1×10^6 4T1 cells suspended in 100 μL of PBS into the right posterior ventral side of each mouse. Upon reaching a tumor volume of ~60 mm^3, the mice bearing 4T1 tumors were randomly assigned to five distinct groups ($n = 5$ mice): (1) control (no treatment), (2) US, (3) MN + US (blank MN + US), (4) mKNN MN (mKNN PNPs-loaded MN), (5) wf-UMP (mKNN MN + US). Under isoflurane anesthesia, MN patches were administered to the mice. The wf-UMP was pressed onto the tumor surface with the thumb. 2 min later, the MNs were completely dissolved, and the wf-UMP was operated with a trigger voltage of 10 Vpp for 5 min on days 0, 1, 2, 3, and 4. Subcutaneous tumor volume and mouse weight were recorded every 2 days. Tumor volumes (mm^3) were calculated using the formula: $V = (\text{length}) \times (\text{width})^2 \times 2^{-1}$. At the end of 14 days of treatment, tumors were harvested and weighted after euthanasia of mice. Subcutaneous tumors and major organs of mice were fixed with 4% formaldehyde and analyzed by H&E staining. Immunofluorescence staining (Ki-67, CD31, TUNEL) was performed on tumor samples from each group. Meanwhile, single-cell suspensions were prepared from mouse subcutaneous tumors for immune FCM. In order to detect MN-induced mircoholes, mice were executed after tumor insertion of MN, and tumors were fixed with 4% paraformaldehyde and then stained with H&E.

In vivo biosafety assessments

To evaluate the biosafety of the wf-UMP, healthy Balb/c mice were randomly divided into 4 groups ($n = 4$ mice): (1) control group; (2) blank MN patch group (MN); (3) mKNN MN patch group (mKNN MN); (4) wf-UMP group (mKNN MN + US). Patches or wf-UMP were applied continuously for the first 5 days of treatment, followed by once-weekly applications thereafter. Skin recovery was recorded on days 0, 3, 6, 10, 14, and 28 post-treatments, and on day 10 and day 28, treated skin samples were collected for H&E staining to assess epidermal thickness. To further assess the in vivo biocompatibility, blood samples were collected from the orbital veins of mice in each group to analyze routine blood and blood biochemical parameters. Major organs (heart, liver, spleen, lung, and kidney) of mice were fixed with 4% formaldehyde and analyzed by H&E staining to assess potential histopathological changes. Transmission electron microscopy (TEM) (JEM-1400FLASH, JEOL) was used to confirm the distribution of mKNN PNPs. Inductively coupled plasma optical emission spectroscopy (ICP-OES) (Thermo ICAP PRO) was used to determine the concentrations of niobium ions.

RNA sequencing

In the above-mentioned subcutaneous tumor experiments in mice, on day 14, tumor samples were collected from the control, mKNN MN, and mKNN+wf-UMP groups using sterile techniques for RNA sequencing. RNA libraries were constructed using Bioanalyzer 2100 and RNA 6000 Nano LabChip Kit (Agilent, CA, USA) following manufacturer' s instructions, ensuring the creation of high-quality RNA sequencing libraries. These libraries were then sequenced using the Illumina Novaseq 6000™ platform (LC-Bio Technology CO., Ltd., Hangzhou, China), generating double-ended reads for subsequent bioinformatics analysis. In order to regulate the false-positive ratio, the p-value modified by the multiple hypothesis testing (Padj) was examined.

FCM analysis

Single-cell suspensions were prepared by digesting isolated tumor tissue or spleen. The immune cells were construed following the standard protocol. To prevent non-specific binding, the cell suspension was incubated with BD Fc Block™ purified anti-mouse CD16/CD32 monoclonal antibody (BD Pharmingen™, Catalog: 553141) for 15 min at 4 °C. Then, cells were stained with surface antibodies: CD45-APC-CY79 (BD Pharmingen™, Catalog: 557659), CD3-BUV395 (BD Pharmingen™, Catalog: 563565), CD4-BUV661 (BD Pharmingen™, Catalog: 741461), CD8-BV711 (BD Pharmingen™, Catalog: 563046), CD49b(BD Pharmingen™, Catalog: 746974), CD44-FITC (BD Pharmingen™, Catalog: 561859), CD62L-PerCP-Cy5.5 (BD Pharmingen™, Catalog: 570282), CD69-PE-CY7 (BD Pharmingen™, Catalog: 552879), CD25-BV786 (BD Pharmingen™, Catalog: 564368), PD-1-BV650 (BD Pharmingen™, Catalog: 744546), CD11B-BV421 (BD Pharmingen™, Catalog: 562605), F4/80-BV605 (BD Pharmingen™, Catalog: 743281), CD86-BUV737 (BD Pharmingen™, Catalog: 741757), Gr-1-BUV496 (BD Pharmingen™, Catalog: 750615), CD11C-BUV563 (BD Pharmingen™, Catalog: 749091), MHC II-R718 (BD Pharmingen™, Catalog: 752163), CD80-BV510 (BD Pharmingen™, Catalog: 740130). Following fixation and permeabilization, cells were stained with intracellular markers: FOXP3-PE (BD Pharmingen™, Catalog: 563101) and CD206-AF647 (BD Pharmingen™, Catalog: 565250). Finally, using BD FACSymphony™ A5 for filtering and detection of stained cells and FlowJo 10.4 for data analysis. Flow cytometry gating strategy involved selecting single cells based on FSC-A/SSC-A, removing dead cells using a viability dye, and identifying specific cell populations through marker expression (e.g., $CD45^+$ for immune cells) (Supplementary Figs. 76 and 77).

Serum collection and enzyme-linked immunosorbent assay

For each group, blood samples were obtained by ocular phlebotomy in dried EP tubes on day 14 after treatments. The upper serum was then centrifuged at 4 °C according to standard steps. The expression levels of cytokines (including IFN-γ, INF-β, IL-6, IL-12P70, and TNF-α) in the sera of mice were detected by a commercial ELISA kit (ZCIBIO Technology, Shanghai, China).

In vivo synergistic immunotherapy

To establish a bilateral tumor model, 1×10^6 4T1 cells were injected into the right abdominal skin of female Balb/C mice. Following a 2 day interval, 5×10^5 4T1 cells were then injected into the left side. After 3 days, the mice were divided into 5 groups ($n = 5$ mice): (1) control (no treatment), (2) US, (3) Anti-PD1, (4) Anti-PD1+mKNN MN (Anti-PD1 + mKNN PNPs-loaded MN), and (5) Anti-PD1+wf-UMP (Anti-PD1+mKNN PNPs-loaded MN + US). The right tumor served as the primary site for synergistic immunotherapy, while the left tumor represented a distant tumor and remained untreated. Following the treatment schematic, Anti-PD1 was injected intraperitoneally to the relevant groups on days 0, 2, and 4 (10 mg kg^{-1} per mouse initially, followed by 5 mg kg^{-1} per mouse for the second and third times). Anti-PD1 antibody was kindly provided by BeiGene, Ltd. Subsequently, both the Anti-PD1+mKNN MN and Anti-PD1+wf-UMP groups underwent treatment with mKNN MN patches consecutively for the first 4 days. Following this, the Anti-PD1+wf-UMP group received an additional US stimulation with wf-UMP (1.2 MHz, 10 Vpp, 5 min). Bilateral tumor volumes and mouse body weights were recorded every 2 days. On the 14th day, spleens and tumors were collected, weighed, and subjected to immune FCM analysis. Similar to the unilateral tumor model, major organs and bilateral tumors were stained for H&E, while bilateral tumors further underwent immunofluorescence (Ki-67, CD31, TUNEL) staining and polychromatic immunofluorescent staining. Simultaneously, serum samples from each group were collected to assess cytokine levels.

Polychromatic immunofluorescent staining

Tumor tissue sections were collected for four-color multiplex fluorescence immunohistochemical staining. Sections were incubated overnight with CD4 (servicebio, Catalog: GB15064, diluted at 1:1000), CD8 (servicebio, Catalog: GB15068, diluted at 1:1000), FOXP3 (servicebio, Catalog: GB112325, diluted at 1:1000) antibodies or F4/80 (servicebio, Catalog: GB113373, diluted at 1:5000), CD86 (servicebio, Catalog: GB115630, diluted at 1:1000), CD163 (servicebio, Catalog: GB113751, diluted at 1:3000) antibodies at 4 °C. Following three washes with PBS, the sections were counterstained with DAPI for nuclei visualization before being sealed. Subsequently, all sections were scanned with a fluorescence scanning camera (Akoya Vectra Polaris).

Tumor rechallenge study

To establish a tumor rechallenge mouse model, 1×10^6 4T1 cells were inoculated into the right abdomen of mice. Five days after inoculation, the mice were treated with the Anti-PD1 antibody in combination with wf-UMP. On day 30 after the end of treatment, 1×10^6 4T1 cells were subcutaneously inoculated into the left abdomen of mice in the combined treatment group and age-matched healthy mice (not inoculated with tumors). After monitoring tumor growth for 15 days, the mice were euthanized and tumors were excised and weighed, and spleens were obtained for FCM analysis.

Inclusion and ethics

Every experiment involving animals have been carried out following a protocol (approve number: 20240514002) approved by an ethical commission of the Animal Care and Use Committee of Sichuan University.

Statistics and reproducibility

Experiments were repeated three times with similar results.

Statistical analysis

Fluorescence images were quantitatively analyzed using ImageJ software (version 1.52a). Data were analyzed using the unpaired, two-tailed Student's *t*-test in GraphPad Prism 9.0 statistical analysis software to determine *p*-values. Survival curves of mice were analyzed using the log-rank (Mantel-Cox) test. Significant differences were defined as $p < 0.05$ ($^*p < 0.05$, $^{**}p < 0.01$, $^{***}p < 0.001$, $^{****}p < 0.0001$).

Reporting summary

Further information on research design is available in the Nature Portfolio Reporting Summary linked to this article.

Data availability

All data supporting the findings of this study are available within the article and its supplementary files. Any additional requests for information can be directed to, and will be fulfilled by, the corresponding authors. Source data are provided with this paper.

References

1. Bray, F. et al. Global cancer statistics 2022: GLOBOCAN estimates of incidence and mortality worldwide for 36 cancers in 185 countries. *CA Cancer J. Clin.* **74**, 229–263 (2024).
2. He, M. et al. Reactive oxygen species-powered cancer immunotherapy: current status and challenges. *J. Control. Release* **356**, 623–648 (2023).
3. Jin, H., Wang, L. Q. & Bernards, R. Rational combinations of targeted cancer therapies: background, advances and challenges. *Nat. Rev. Drug Discov.* **22**, 213–234 (2023).
4. Wang, K. et al. The mechanism of piezocatalysis: energy band theory or screening charge effect? *Angew. Chem. Int. Ed.* **61**, e202110429 (2022).
5. Wu, A. et al. Ultrasound-driven piezoelectrocatalytic immunoactivation of deep tumor. *Adv. Sci.* **10**, 2303016 (2023).
6. Xu, Q. et al. Construction of bio-piezoelectric platforms: from structures and synthesis to applications. *Adv. Mater.* **33**, 2008452 (2021).
7. Hu, H. et al. Emerging nanomedicine-enabled/enhanced nanodynamic therapies beyond traditional photodynamics. *Adv. Mater.* **33**, 2005062 (2021).
8. Fan, Y. et al. Biomimetic piezoelectric nanomaterial-modified oral microrobots for targeted catalytic and immunotherapy of colorectal cancer. *Sci. Adv.* **10**, eadm9561 (2024).
9. Chang, H. et al. Cryomicroneedles for transdermal cell delivery. *Nat. Biomed. Eng.* **5**, 1008–1018 (2021).
10. Tehrani, F. et al. An integrated wearable microneedle array for the continuous monitoring of multiple biomarkers in interstitial fluid. *Nat. Biomed. Eng.* **6**, 1214–1224 (2022).
11. Hu, H. et al. Stretchable ultrasonic transducer arrays for three-dimensional imaging on complex surfaces. *Sci. Adv.* **4**, eaar3979 (2018).
12. Zhou, S. et al. Transcranial volumetric imaging using a conformal ultrasound patch. *Nature* **629**, 810–818 (2024).
13. Liu, H. et al. Wearable bioadhesive ultrasound shear wave elastography. *Sci. Adv.* **10**, eadk8426 (2024).
14. Hu, H. et al. A wearable cardiac ultrasound imager. *Nature* **613**, 667–675 (2023).
15. Wang, C. et al. Monitoring of the central blood pressure waveform via a conformal ultrasonic device. *Nat. Biomed. Eng.* **2**, 687–695 (2018).
16. Lin, M., Hu, H., Zhou, S. & Xu, S. Soft wearable devices for deep-tissue sensing. *Nat. Rev. Mater.* **7**, 850–869 (2022).
17. Hu, H. et al. Stretchable ultrasonic arrays for the three-dimensional mapping of the modulus of deep tissue. *Nat. Biomed. Eng.* **7**, 1321–1334 (2023).
18. Lin, M. et al. A fully integrated wearable ultrasound system to monitor deep tissues in moving subjects. *Nat. Biotechnol.* **42**, 448–457 (2023).
19. Zhang, L. et al. A conformable phased-array ultrasound patch for bladder volume monitoring. *Nat. Electron.* **7**, 77–90 (2024).

20. Yang, Y. et al. Improved pharmacodynamics of epidermal growth factor via microneedles-based self-powered transcutaneous electrical stimulation. *Nat. Commun.* **13**, 6908 (2022).
21. Xiang, Y. et al. Ultrasound-triggered interfacial engineering-based microneedle for bacterial infection acne treatment. *Sci. Adv.* **9**, eadf0854 (2023).
22. Huang, Y. et al. Ultrasound-activated piezo-hot carriers trigger tandem catalysis coordinating cuproptosis-like bacterial death against implant infections. *Nat. Commun.* **15**, 1643 (2024).
23. Yuk, H. et al. Dry double-sided tape for adhesion of wet tissues and devices. *Nature* **575**, 169–174 (2019).
24. Wang, C. et al. Bioadhesive ultrasound for long-term continuous imaging of diverse organs. *Science* **377**, 517–523 (2022).
25. Jiang, L. et al. Flexible ultrasound-induced retinal stimulating piezo-arrays for biomimetic visual prostheses. *Nat. Commun.* **13**, 3853 (2022).
26. Xu, S. et al. Stretchable batteries with self-similar serpentine interconnects and integrated wireless recharging systems. *Nat. Commun.* **4**, 1543 (2013).
27. Yu, X. et al. Skin-integrated wireless haptic interfaces for virtual and augmented reality. *Nature* **575**, 473–479 (2019).
28. Jiang, Y. et al. Wireless, close-loop, smart bandage with integrated sensors and stimulators for advanced wound care and accelerated healing. *Nat. Biotechnol.* **41**, 652–662 (2023).
29. Nelson, T. R., Fowlkes, J. B., Abramowicz, J. S. & Church, C. C. Ultrasound biosafety considerations for the practicing sonographer and sonologist. *J. Ultrasound Med.* **28**, 139–150 (2009).
30. Bigelow, T. A. et al. The thermal index: Its strengths, weaknesses, and proposed improvements. *J. Ultrasound Med.* **30**, 714–734 (2011).
31. Chen, Z. et al. A piezoelectric-driven microneedle platform for skin disease therapy. *Innovation* **5**, 100621 (2024).
32. Shao, J., Li, X., Li, Y., Lin, J. & Huang, P. Self-heating multistage microneedle patch for topical therapy of skin cancer. *Adv. Mater.* **36**, 2308217 (2024).
33. Liao, J. et al. Boosting piezo-catalytic activity of KNN-based materials with phase boundary and defect engineering. *Adv. Funct. Mater.* **33**, 2303637 (2023).
34. Sun, X. et al. Modulating polarization rotation to stimulate the high piezocatalytic activity of (K, Na)NbO_3 lead-free piezoelectric materials. *Appl. Catal. B-Environ.* **313**, 121471 (2022).
35. Bandi, S. et al. Crystallite size induced bandgap tuning in WO_3 derived from nanocrystalline tungsten. *Scr. Mater.* **176**, 47–52 (2020).
36. Tu, S. et al. Piezocatalysis and piezo-photocatalysis: catalysts classification and modification strategy, reaction mechanism, and practical application. *Adv. Funct. Mater.* **30**, 2005158 (2020).
37. Liu, W. et al. Directing charge transfer in a chemical-bonded $BiTiO_3$@ReS_2 schottky heterojunction for piezoelectric enhanced photocatalysis. *Adv. Mater.* **34**, 2202508 (2022).
38. Gong, N. et al. Carbon-dot-supported atomically dispersed gold as a mitochondrial oxidative stress amplifier for cancer treatment. *Nat. Nanotechnol.* **14**, 379–387 (2019).
39. Guan, X. et al. Nanoparticle-enhanced radiotherapy synergizes with PD-L1 blockade to limit post-surgical cancer recurrence and metastasis. *Nat. Commun.* **13**, 2834 (2022).
40. Chen, X. et al. Chemically programmed STING-activating nanoliposomal vesicles improve anticancer immunity. *Nat. Commun.* **14**, 4584 (2023).
41. Wang, D. et al. Metal-cyclic dinucleotide nanomodulator-stimulated STING signaling for strengthened radioimmunotherapy for large tumor. *Small* **18**, 22033227 (2022).
42. Kumagai, S. et al. The PD-1 expression balance between effector and regulatory T cells predicts the clinical efficacy of PD-1 blockade therapies. *Nat. Immunol.* **21**, 1346–1358 (2020).
43. Kurachi, M. $CD8^+$ T cell exhaustion. *Semin. Immunopathol.* **41**, 327–337 (2019).
44. Wang, T. et al. A cancer vaccine-mediated postoperative immunotherapy for recurrent and metastatic tumors. *Nat. Commun.* **9**, 1532 (2018).
45. Libanori, A., Chen, G., Zhao, X., Zhou, Y. & Chen, J. Smart textiles for personalized healthcare. *Nat. Electron.* **5**, 124–156 (2022).
46. Wang, C. & Zhao, X. See how your body works in real time-wearable ultrasound is on its way. *Nature* **630**, 817–819 (2024).
47. Zhou, T. et al. 3D printable high-performance conducting polymer hydrogel for all-hydrogel bioelectronic interfaces. *Nat. Mater.* **22**, 895–902 (2023).
48. Arwani, R. T. et al. Stretchable ionic-electronic bilayer hydrogel electronics enable in situ detection of solid-state epidermal biomarkers. *Nat. Mater.* **23**, 1115–1122 (2024).
49. Li, B. et al. Photothermal therapy of tuberculosis using targeting pre-activated macrophage membrane-coated nanoparticles. *Nat. Nanotehcnol.* **19**, 834–845 (2024).
50. Li, Z., Wang, Y., Gu, Z. & Hu, Q. Engineering cells for therapy and diagnosis. *Nat. Rew. Bioeng.* **2**, 770–784 (2024).

Acknowledgements

This work is supported by National Science Foundation of China (U23A20567 and 52202144), Sichuan Provincial Science and Technology Department Key Research and Development Program (2024YFHZ0004), and Natural Science Foundation of Sichuan Province (2024NSFSC0231 and 2024NSFJQ0025).

Author contributions

L.J. and J.W. conceived and designed experiments. H.X. prepared the piezoelectric materials and devices and conducted tests, data collection, and analysis. J.J., X.H., and K.C. conducted in vitro and in vivo experiments. X.H. prepared the bioadhesive hydrogel. X.H. and G.L. performed simulations by COMSOL Multiphysics. Z.T. performed DFT calculations using VASP. Y.Z. conducted the acoustic field test. H.X., J.J. and L.J. wrote the manuscript. J.W., L.J., X.P., Y.S., and X.H. supervised the work. All authors discussed and commented on the manuscript.

Competing interests

The authors declare no competing interests.

Additional information

Supplementary information The online version contains supplementary material available at https://doi.org/10.1038/s41467-025-58075-z.

Correspondence and requests for materials should be addressed to Xingchen Peng, Laiming Jiang or Jiagang Wu.

Peer review information *Nature Communications* thanks M. Amin Karami, Shayan F. Lahiji, and the other, anonymous, reviewer(s) for their contribution to the peer review of this work. A peer review file is available.